Research Square

Preprints are preliminary reports that have not undergone peer review.
They should not be considered conclusive, used to inform clinical practice,
or referenced by the media as validated information.

# An aerosol dry deposition theory connects landcover geometry to climate

**Jingkun Jiang**

jiangjk@mail.tsinghua.edu.cn

Tsinghua University https://orcid.org/0000-0001-6172-190X

**Junchen Guo**

Tsinghua University

**Ganzhen Chen**

National University of Defense Technology

**Xinyan Zhao**

Tsinghua University

**Shengzhen Zhou**

Sun Yat-sen University

**Shixin Mai**

Sun Yat-sen University

**Minghao Wang**

Tsinghua University

**Runlong Cai**

Fudan University https://orcid.org/0000-0002-6630-0896

**Yijing Chen**

Tsinghua University

**Haiyan Yue**

Guangzhou meteorological bureau

**Taofeng Gu**

Guangzhou meteorological bureau

**Hao Wu**

Chengdu University of Information Technology

**Douglas Worsnop**

Aerodyne Research Inc. https://orcid.org/0000-0002-8928-8017

**Jiandong Wang**

Nanjing University of Information Science and Technology https://orcid.org/0000-0003-3000-622X

**Physical Sciences - Article**

**Keywords:**

**Posted Date:** September 21st, 2026

**DOI:** https://doi.org/10.21203/rs.3.rs-10972670/v1

**License:** This work is licensed under a Creative Commons Attribution 4.0 International License.
Read Full License

**Additional Declarations:** There is **NO** Competing Interest.

# An aerosol dry deposition theory connects landcover geometry to climate

Junchen Guo[1], Ganzhen Chen[3], Xinyan Zhao[1], Shengzhen Zhou[4], Shixin Mai[4], Minghao Wang[1], Runlong Cai[5], Yijing Chen[1], Haiyan Yue[7], Taofeng Gu[7], Hao Wu[6], Douglas R. Worsnop[8,9], Jiandong Wang[2], Jingkun Jiang[1]

[1] State Key Joint Laboratory of Environment Simulation and Pollution Control, School of Environment, Tsinghua University, Beijing, China.
[2] State Key Laboratory of Climate System Prediction and Risk Management, Nanjing University of Information Science and Technology, Nanjing 210044, China
[3] College of Meteorology and Oceanography, National University of Defense Technology, Changsha, 410073, China
[4] School of Atmospheric Sciences, Guangdong Provincial Observation and Research Station for Climate Environment and Air Quality Change in the Pearl River Estuary, Sun Yat-sen University, Zhuhai, 519082, China.
[5] Shanghai Key Laboratory of Air Quality and Environmental Health, Department of Environmental Science & Engineering, Fudan University, Shanghai, China.
[6] Key Laboratory of China Meteorological Administration Atmospheric Sounding, College of Electronic Engineering, Chengdu University of Information Technology, Chengdu 610225, China.
[7] Guangzhou meteorological bureau, Guangzhou, China.
[8] Aerodyne Research Inc., Billerica, Massachusetts 01821, USA.
[9] Institute for Atmospheric and Earth System Research/Physics, University of Helsinki, 1100014 Helsinki, Finland.

**Correspondence to:**

Jiandong Wang, jiandong.wang@nuist.edu.cn

Jingkun Jiang, jiangjk@tsinghua.edu.cn

**Abstract**

Landcover geometry perturbs atmospheric aerosol loading and hence the Earth's energy budget through aerosol dry deposition (ADD). However, this climate effect remains elusive due to the knowledge gap in the relationship between landcover geometry and ADD. Here, we integrate remote sensing, ground observations and laboratory experiments to show that ADD is enhanced first and then weakened with increasing total geometric area of soil(water), vegetations and buildings per unit ground (i.e., $A_L$). This "area law" for ADD cannot be explained by the resistance model prevailing for half a century. We therefore develop phase-wise migration theory by reconstructing ADD physical framework from multi-scale fluid dynamics and aerosol dynamics.

All parameters in the reconstructed framework have definite physical meaning and are measured or theoretically derived, making the framework capable of predicting ADD velocity without any fitting to observed ADD velocity. This new paradigm completely supported by fundamental dynamics surpasses the current semi-empirical paradigm where resistance model predicts ADD velocity only after fitting itself to observed ADD velocity. As a result, our theory not only well explains the observed "area law" but also decreases observation-prediction discrepancy in ADD velocity from factors of 50-100 to a factor of 8. Coupling the new framework into the Community Earth System Model reveals that considering landcover geometry changes ADD velocity to 0.16-23 times the original value, which further changes mean terrestrial aerosol cooling effect by 30%-60%. Our findings may provide new perspectives for land-based climate adaptation which almost always introduces landcover geometric modification.

**Introduction**

Landcover geometry, such as leaf area or leaf surface roughness, modulates atmospheric aerosol loading and ecosystem nutrient input through aerosol dry deposition (ADD)[1-4]. Thus, figuring out the relationship between landcover geometry and ADD is crucial for an advanced understanding of ecosystem productivity, air pollution, and climate system. However, although existing research has revealed the dependence of ADD on aerosol diameter and in-situ friction velocity[5-7], how landcover geometry influences ADD has remained elusive for almost half a century since ADD was widely concerned.

Exploration of the relationship between ADD and landcover geometry has been persistently impeded by two bottlenecks: noises from other ADD drivers and challenges in clarifying dynamics underlying ADD. Measuring ADD velocity from aerosol flux observations for real landcover is a significant way to study ADD. However, under such uncontrolled conditions, ADD velocity is simultaneously influenced by aerosol diameter, in-situ friction velocity, and landcover geometry[8,9]. As a result, remarkable noise from uncontrolled aerosol diameter and in-situ friction velocity buries the true relationship between ADD and landcover geometry. Another promising avenue lies in resolving the mechanistic link between landcover geometry and ADD through governing dynamics. However, complexity of multi-scale aerosol motions driven by multiple mechanisms during deposition makes the establishment of an ADD physical framework a daunting challenge. The currently prevalent ADD framework established by Slinn et al. 1982 (i.e., resistance model) contains substantial uncertainty as it was built on an over-simplified physical scenario and several improper empirical analogies[10]. This model analogizes ADD to electrical circuits where ADD flux is regarded as "current" and is determined by "resistance". However, the most important parameter in the resistance model, surface resistance, can only be obtained by fitting the model to observed ADD velocity[10-12]. Although some researchers have been tuning the surface resistance based on different ADD velocity observations over the past half century[11-14], the resistance model still fails to reveal the true relationship between landcover geometry and ADD due to the inherent limitations of its semi-empirical framework.

Here, we provide a comprehensive understanding of the role that landcover geometry plays in ADD from angles of both data and basic dynamics. On the data front, we synthesize atmospheric aerosol flux observations, landcover geometry data, and controlled laboratory deposition

experiments to unmask the hidden relationship between landcover geometry and ADD. On the dynamics front, we develop phase-wise migration theory (PWM theory) by reconstructing ADD physical framework from aerosol dynamics and multi-scale fluid dynamics. The new ADD framework successfully explains the observed relationship between landcover geometry and ADD at a fundamental level. In the end, multiple implications of our findings for the climate system, ecosystem and air pollution are also discussed.

## Result

### Unmasking the hidden relationship between aerosol dry deposition and landcover geometry from multi-type data

Landcover can be approximately described as a geometric structure composed of soil (water), vegetations and buildings. Here, we characterize landcover geometry through two parameters, landcover geometric area per unit ground ($A_L$, $m^2$ $m^{-2}$) and landcover micro roughness ($k_L$, mm). Landcover geometric area refers to the total external surface area of soil (water), vegetations and buildings. Thus, $A_L$ highly depends on vegetation geometric area per unit ground ($A_v$, Methods) and building geometric area per unit ground ($A_b$, Methods). Typically, $A_L$ values for bare land, forest and urban are 1, 1.1-13, and 1.1-3. Landcover micro roughness, $k_L$, refers to the average size of tiny bumps smaller than viscous scale (i.e., total thickness of viscous sublayer and buffer layer, several millimeters under typical atmospheric conditions) in the external surface of soil (water), vegetations or buildings. In this study, values of $k_L$ are obtained from reported surface data of different materials. Typically, $k_L$ values for bare land, forest and urban are 1-1000 μm (ranging from clay to asphalt)[15], 5-30 μm (a typical range for leaves)[16,17], and 50-200 μm (a typical range for building exterior walls)[18]. The geometric characterization for different landcover types is shown in Extended Data Fig. 1.

Landcover includes canopy-free landcover (such as water/bare land) and canopy-containing landcover (such as forest or urban). For canopy-free landcover, the impact of landcover geometry on ADD has been directly observed in controlled laboratory deposition experiments. Geometry of canopy-free landcover is primarily characterized by $k_L$ (i.e., $A_L$ keeps ~1) and generally represented by inner surfaces of wind tunnels with different micro roughness in reported controlled deposition experiments (Methods). Some experimental results show that increasing $k_L$ can remarkably enhance ADD velocity by a factor of ~10 [19,20] (Extended Data Fig. 2). For canopy-containing landcover, however, directly observing the impact of landcover geometry on ADD in controlled experiments is practically unfeasible due to difficulties in modeling canopies (such as forests or cities) in a laboratory. Consequently, empirical researches in the relationship between landcover geometry and ADD relied almost exclusively on atmospheric aerosol flux observations. In such observations, however, ADD is also significantly influenced by aerosol diameter ($D_p$) and in-situ friction velocity ($u^*$). As Fig.1a shows, $D_p$ is able to cause observed ADD velocity to vary by a factor of up to ~100 in existing atmospheric aerosol flux observations. As a result, remarkable noise from uncontrolled $D_p$ and $u^*$ in atmospheric observations buries the true relationship between ADD and landcover geometry.

To overcome this difficulty, we introduce denoised ADD intensity which is defined as the ratio of ADD velocity over targeted landcover to that over reference landcover at the same $D_p$ and $u^*$.

This indicator substantially reduces noise from $D_p$ and $u^*$ through fixing the two ADD drivers. Because ADD over canopy-free landcover has been well researched in controlled deposition experiments (Methods), the reference landcover is determined as a specific canopy-free landcover ($A_L$=1, $k_L$=1 μm) in this study. The ADD velocity over reference landcover at various $D_p$ and $u^*$ is obtained from a one-dimensional Eulerian ADD model (Methods), which well predicts observed dependence of ADD velocity on $k_L$, $D_p$ and $u^*$ in laboratory studies (Extended Data Figs. 2-4).

In this study, observation-based denoised ADD intensity is calculated for 14 sites around the world where canopies exist and aerosol flux observations (size-resolved) are available. To the best of our knowledge, the calculation includes all published atmospheric aerosol flux measurements (size-resolved) with available landcover geometry data. Observed ADD velocity for calculating denoised ADD intensity is shown in Fig. 1a. ADD velocity values in site 1 are obtained from the first aerosol flux observation over a built-up region conducted in this study while ADD velocity values in other sites are collected from published aerosol flux observations over vegetated regions (Methods). Values of $A_L$ for the 14 sites are calculated based on five remote sensing data sets and ground observations (if existing), to make our findings robust. As shown in Fig. 1b, the observed denoised ADD intensity highly depends on $A_L$. It is found that the observed denoised ADD intensity rapidly increases from ~1 to ~35 as $A_L$ goes up from ~1.4 at a grass land in Britain to ~3.5 at a needle leaf forest in Israel. However, the observed denoised ADD intensity then decreases to ~1.8 with continued increase of $A_L$ to ~10.3 at a needle leaf forest in America. We also find that the observed denoised ADD intensity of a built-up region is relatively larger than that of a vegetated region at similar $A_L$ values, which should be attributed to larger $k_L$ of the built-up region (building external surfaces are generally much rougher than vegetation external surfaces).

Almost all ADD modules in current atmospheric/Earth system models[14,21,22] adopt Slinn's resistance model where eight free parameters are obtained by fitting the model to observed ADD velocity (mainly including atmospheric flux observations, with limited laboratory data being chosen). An introduction of the resistance model is provided in Methods. Conventional parameters provided by Zhang et al. 2001[11] are the default option in most existing atmospheric/Earth system models while refitted parameters recently provided by Emerson et al. 2020 [12] are also increasingly used. However, whether with conventional parameters or refitted parameters, resistance model fails to explain the observed remarkable dependence of ADD on $k_L$ and $A_L$ (Extended Data Fig.2 and Fig. 1b). This failure, which is rooted in the semi-empirical nature of the model itself rather than in parameter uncertainty, emphasizes the necessity of understanding ADD at a fundamental level.

**Phase-wise migration theory**

We propose phase-wise migration (PWM) theory to fundamentally understand the observed dependence of ADD on landcover geometry. Derived from aerosol dynamics and multi-scale fluid dynamics, this theory reconstructs ADD physical framework and describes how $A_L$ and $k_L$ regulate aerosol trapping sites and atmospheric motion to intervene aerosol migration ranging from sub-millimeter scale to tens of meters scale. The core conception of the reconstructed framework is to divide the whole ADD process into different phases based on dominant aerosol motion mechanisms. ADD is driven by force field and aerosol collisions with ambient air molecules. In

real atmosphere, gravitational field is the primary force field relevant to ADD and induces an aerosol motion mechanism named gravitational settling[23]. This mechanism is dictated chiefly by aerosol diameter. In contrast, the aerosol collisions with ambient air molecules induce three aerosol motion mechanisms named air entrainment, Brownian motion, and turbophoresis respectively[23,24]. Air entrainment refers to the aerosol motion driven by aerosol-air collisions induced by the directional motion of air molecules (i.e., advection and turbulence). This mechanism is mainly determined by atmospheric motion. Brownian motion refers to the aerosol motion driven by aerosol-air collisions induced by thermal motion of air molecules. This mechanism is governed primarily by aerosol diameter. Turbophoresis refers to the aerosol motion driven by imbalanced collisions from air molecules in heterogeneous turbulence, that is, the phenomenon that air molecules from stronger turbulence transfer more momentum to aerosols by collisions and therefore force aerosols to move along the direction where turbulence weakens. This mechanism is mainly determined by both aerosol diameter and atmospheric motion.

Atmospheric motion remarkably varies along an ADD path[25], significantly influencing dominant aerosol motion mechanisms in the path. Thus, we divide the whole ADD into three phases according to differences in dominant aerosol motion mechanisms: ADD in inertial sublayer, ADD in drag domain, and ADD in viscous domain (Fig. 2a, drag domain and viscous domain are collectively referred to as roughness sublayer). Drag domain and viscous domain are the subspaces of roughness sublayer (bottom of surface layer) defined in this study. Inertial sublayer includes the space above landcover where Monin-Obukhov similarity theory is valid and atmosphere motion is characterized by constant turbulent stress. Drag domain only exists when landcover includes canopies. We define drag domain as the space unoccupied by vegetations/buildings in a canopy where atmospheric motion is dominantly driven by turbulent stress and drag force induced by vegetations/buildings. Viscous domain includes viscous sublayer and buffer layer (millimeter-scale in general) on the external surfaces of ground/vegetations/buildings, where atmospheric motion is dominantly driven by turbulent stress and viscous stress. Dominant aerosol motion mechanisms for the three phases are determined by scale analysis (Methods and Extended Data Fig. 5). According to the new ADD physical framework (Fig. 2a), we provide a new mathematical expression of ADD velocity and its derivation (Methods, Extended Data Fig. 9, and Supplementary). It should be noticed that mentioned one-dimensional Eulerian ADD model is a special case of the proposed framework.

One critical contribution of PWM theory is to reveal the physical origin of ADD dependence on $A_L$ and $k_L$. Increasing $k_L$ value can shorten aerosol migration distance in viscous domain by adjusting position of trapping sites (Fig. 2a), which effectively enhances ADD. This effect satisfactorily accounts for the observed ADD dependence on $k_L$ (Extended Data Fig. 2). Compared with $k_L$, the $A_L$ effect on ADD is much more complicated. On the one hand, increasing $A_L$ enhances ADD by directly increasing trapping sites; On the other hand, increasing $A_L$ weakens ADD by suppressing atmospheric motion in drag domain and viscous domain (hence slowing down aerosol migration in the two phases). This double effect well explains the observed ADD dependence on $A_L$ (Fig. 1c). The suppression effect of $A_L$ on atmospheric motion is characterized by wind attenuation coefficient (Extended Data Fig. 6). Larger wind attenuation coefficient means stronger suppression effect (Supplementary, section 3). For vegetated regions, the double effect of $A_L$ (only

contributed by ground and vegetations) causes denoised ADD intensity to rise first and then fall as $A_L$ increases. For built-up regions, however, our framework predicts that denoised ADD intensity decreases with increasing $A_L$ (only contributed by ground and buildings). The reason is that the stronger effect of added buildings on suppressing atmospheric motion overwhelms their effect on providing aerosol trapping sites, which can be supported by higher wind attenuation coefficient of buildings at given $A_L$ values (Fig. 1c).

The comparison between performance in predicting ADD velocity of the proposed ADD framework and resistance model are presented in Fig.2 b-d. Compared to resistance model, the new framework decreases observation-prediction discrepancy (including both controlled laboratory deposition experiments and atmospheric flux observations) from factors of 50-100 to a factor of 8 and increases observation-prediction consistency from $R^2$=0.09-0.41 to $R^2$=0.78. These results highlight the importance of landcover geometry and fundamental understanding of ADD. In addition, considering that previous works focused extensively on modeling dependence of ADD over real landcover on aerosol diameter, we specifically present the relevant performance of the proposed framework in Supplementary Fig. S1 and Supplementary Fig. S2. Besides these quantitative improvements, more importantly, PWM theory turns the way of understanding ADD from a semi-empirical paradigm to a paradigm completely supported by fundamental dynamics. All parameters in our ADD framework have definite physical meanings and are measured or theoretically derived (Extended Data Table 1), making the framework capable of predicting ADD velocity without any fitting to observed ADD velocity. In contrast, resistance model predicts ADD velocity only after fitting itself to observed ADD velocity. Thus, PWM theory possesses stronger ability to explain and predict ADD than the resistance model. Furthermore, PWM theory also provides a much more open framework to understand ADD (Fig. 3). According to the old framework from resistance model, progress of ADD understanding could only come from one path: more atmospheric flux observations to fit better empirical parameters in this model. In contrast, our new framework opens up additional five independent yet convergent avenues. In addition to direct flux observations, advances in macroscale landcover observations (e.g., leaf area index, building height), microscale landcover characterization (e.g., surface roughness of different materials), multi-scale fluid dynamics, aerosol dynamics, and controlled deposition experiments will all directly contribute to improving the understanding of ADD.

Despite these advantages, the remaining observation-prediction discrepancy of a factor of ~8 indicates the necessity to further clarify ADD physics. This discrepancy likely stems from uncertainty in measurements or in theoretical calculations for parameters in the proposed framework (Extended Data table 1). For example, indirect micro roughness measurements (obtained from reported measurements of different materials) or limitations in remote sensing technique (such as cloud interference) may introduce uncertainty to $k_L$ and $A_L$ while inadequate knowledge in aerosol dynamics (such as the precise expression of turbophoresis) and multi-scale fluid dynamics (such as in-canopy thermal turbulence) likely introduce uncertainty to parameters characterizing aerosol motion in roughness sublayer (such as ε or parameters in $V_{tc}^{+}$, see Extended Data Table 1 and Supplementary). This means single discipline can no longer cope with current challenges in understanding ADD and interdisciplinary cooperation is necessary. In such a context, the proposed framework is a powerful tool for integrating future progresses of multiple related

disciplines such as land observation, surface property of different materials, aerosol dynamics, and multi-scale fluid dynamics.

**Multiple implications**

To further explore the role of landcover geometry in the Earth system, we develop a new ADD module underlain by PWM framework and couple it into the Community Earth System Model (CESM). By leveraging this proposed module, we quantify multiple influences of landcover geometry on global ADD velocity, global column aerosol mass, and global aerosol forcing ($RF_a$) in Fig. 4. These results are obtained by comparing the scenario considering landcover geometry predicted by the new ADD module with the scenario ignoring landcover geometry predicted by the traditional ADD module (i.e., resistance model). All simulations are performed by using emission conditions, meteorological conditions and landcover conditions during 2018-2020. Given that major climate reports (e.g., IPCC AR6) are based on the traditional ADD module with conventional parameters, we employ this baseline scheme to simulate the scenario omitting landcover geometry (Fig. 4). We also provide the simulation in which the scenario ignoring landcover geometry is predicted by the traditional ADD module with refitted parameters (Extended Data Fig. 7). Fig. 4 only presents the optimal estimation of multiple impacts of landcover geometry. The optimal estimation means that input landcover geometry parameters in the new ADD module meet: (1) values of $A_L$ are taken as averages of results calculated from different remote sensing data sets; (2) values of $k_L$ for ground, vegetations or buildings are taken as the optimal values that generate modeled ADD velocity agreeing best with observations within the measured $k_L$ range of corresponding materials. Multiple impacts of landcover geometry most favorable or unfavorable to ADD under observational constraint are estimated to quantify the uncertainty arising from landcover geometry input (Fig. S7 and Fig. S8). To ensure that the estimated multiple impacts of landcover geometry represent real physical feedback rather than numerical artifacts from model coupling, we compare the ground-level $PM_{2.5}$ concentrations simulated by both the new and traditional ADD modules with satellite retrievals[26]. The $PM_{2.5}$ concentrations simulated by the new ADD module correlate reasonably well with satellite observations ($R^2$=0.36, Fig. S9), comparable to the traditional module ($R^2$=0.32). This reasonable consistency between simulations and observations supports the physical rationality of our simulations.

As shown in Fig. 4a, landcover geometry causes global ADD velocity values to vary dramatically, reaching 0.16-23 times the original values. The most remarkable enhancement of ADD velocity induced by landcover geometry occurs within the forest zone ranging from 40°N to 60°N in Eurasia. $A_L$ here is distributed between 3 and 7 $m^2$ $m^{-2}$ where landcover geometry is most favorable to ADD (Fig. 1c). In contrast, the most remarkable suppression of ADD velocity induced by landcover geometry occurs at the Amazon forest and Greenland. $A_L$ here is distributed between 9 and 13 $m^2$ $m^{-2}$ or between 0 and 2 $m^2$ $m^{-2}$, where landcover geometry is most unfavorable to ADD (Fig. 1c). Considering that ADD controls nutrient input into ecosystems (nutrient input from ADD is changed by a range from -85% to 768% when landcover geometry is considered), our work may facilitate a more comprehensive understanding of global biodiversity[27], ecosystem productivity[28], and ecosystem stability[29]. The remarkable changes in global ADD velocity induced by landcover geometry directly lead to variations in global column aerosol mass by a range from -83% to +13% (Fig. 4b) and variations in ground level $PM_{2.5}$ concentration by a range from -73%

to +139% (Fig. S10). This may imply a potential relationship between regional haze pollution and landcover geometry. The remarkable changes in global aerosol loading further result in significant changes in global aerosol forcing ($RF_a$). Fig. 4c shows the absolute changes in global $RF_a$ induced by landcover geometry. It is found that noticeable changes larger than +4W $m^{-2}$ occur in Northern Africa, East Asia, Southeast Asia, and Australia. Overall, the mean terrestrial aerosol cooling effect is reduced by 46%, with a variation range from 30% to 60% caused by landcover geometry uncertainty (Fig. S7 and Fig. S8). Fig. 4d shows the relative changes (the relative changes only reflect the degree of change, not the increase or decrease) in global $RF_a$ induced by landcover geometry. It is found that global $RF_a$ at the grid scale (2.5°×1.9°), a scale relevant to extreme weather, can change by more than 1000%. Given that the local radiative budget plays a significant role in extreme weather[30,31], landcover geometry may be a critical driver for extreme weather.

We emphasize that the estimated 30%–60% change in mean terrestrial aerosol forcing does not necessarily invalidate current mainstream estimates (e.g., IPCC AR6), which also integrate multi-platform observational constraints. Furthermore, the absolute magnitude of modeled aerosol forcing is subject to compounded uncertainties across various modules, such as emissions, transport, aerosol-cloud interactions, wet deposition and radiative transfer. However, rather than claiming an absolute value of aerosol forcing, our modeling experiments serve as a targeted sensitivity test to quantify the isolated impact of a previously missing physical mechanism. By holding other modules constant, we find that landcover geometry modulation of atmospheric motion and aerosol trapping sites dramatically change terrestrial aerosol forcing by 30%–60%. This high sensitivity of the Earth's energy budget to landcover geometry has been entirely overlooked in traditional land-atmosphere interaction frameworks. This finding is particularly crucial for future climate adaptation. Currently, nature-based solutions, such as working land management, afforestation, wetland expansion and green-infrastructure investment, are considered a promising path for climate adaptation in the warming future. Implementation of a nature-based solution almost always brings changes in landcover geometry, which either enhance or weaken the effectiveness of the implemented nature-based solution. However, the influence of landcover geometry on the effectiveness of nature-based solutions has never been considered. For example, Girardin et al. 2021[32] argue that conventional nature-based solutions are able to cause ~0.3°C reduction in mean global temperature toward the end of this century if temperature rise since preindustrial times peaks at 2°C. This estimation likely deviates from the real effectiveness of conventional nature-based solutions due to ignoring landcover geometry changes. Our findings not only significantly improve current understanding of the Earth system but also provide new perspectives for climate adaptation.

## Method

### Calculation of vegetation geometric area per unit ground

Vegetation geometric area per unit ground ($A_V$, $m^2$ $m^{-2}$) refers to total external surface area of leaves, stems and branches of vegetations per unit ground. However, published ecological measurements have shown that leaf area[33] dominates $A_V$. Thus, in this work, we assume $A_V$ is dominated by leaf area and express it as: $A_V = 2*LAI$. LAI denotes leaf area index which is defined as one-sided leaf surface area per unit ground. There are two types of the LAI data, ground observations and satellite remote sensing. The ground observation data are more accurate but have extremely low spatial/ temporal coverage, while the satellite remote sensing data have relatively lower accuracy but high spatial/temporal coverage. Currently, state-of-the-art remote sensing LAI products agree well with ground observations, with deviation generally less than 100%. In this study, LAI data form both ground observations (only for aerosol flux observation sites, if exists) and satellite remote sensing are used. Satellite remote sensing LAI data used in this work come from three widely used LAI products, named GLASS[34], MUSES[35], and GEOV2[36], to ensure robustness of our results. The three products use machine leaning techniques to fuse LAI data calculated from different sensors and radiative transfer models, therefore performing better than LAI products from single sensor and radiative transfer model (e.g., MODIS[37], CYCLOPES[38], or GLOBCARBON[39]). Spatial resolutions of LAI products used for calculating $A_V$ or $A_L$ of aerosol flux observation sites are 500m, 500m, and 1000m for GLASS, MUSES, and GEOV2 respectively. The reason for this chose is that the effective region influencing measured ADD velocity of an observation site covers 300-3000m radius around the site (See explanation later in section "Calculation of effective landcover geometric area per unit ground for an observation site").

### Calculation of building geometric area per unit ground

Building surface area ($A_b$, $m^2$ $m^{-2}$) refers to the total external surface area of buildings per unit ground. This parameter is estimated based on high-resolution building height data in this study. We use two remote sensing datasets of building height to obtain robust estimation of $A_b$. To the best of our knowledge, the selected data sets are the only two building height data sets which cover the whole China and have a high spatial resolution of less than or equal to 100m (a scale smaller than or comparable to individual buildings). The first dataset is provided by Wu et al. 2023[40]. This dataset has a spatial resolution of ~10m and is generated by a random forest regression model trained by building height reference data, radar data, optical data, night-time light data, population data and topographic data. The building height reference data used for training are established based on building floor number for 62 cities in China for the year 2018 from Baidu map services. Other training data are mainly remote sensing information from Sentinel-1, Sentinel-II, Phased Array Type L-band Synthetic Aperture Radar (PALSAR) and LUOJIA 1–01(the nighttime light data satellite). The second building height dataset are provided by Li et al. 2024[41]. This data set has spatial resolution of ~100 m and is generated by a multi-task deep learning model trained by other building height reference data and satellite images. The building height reference data used for training are generated through a radar-based global digital elevation model (TDX-DEM) and urban area outlined by the Gridded Population of the World, Version 4(GPWv4) dataset and the

Global Human Settlement-Urban Centre Database (GHS-UCDB). The training satellite images include (1) VV and VH polarizations from Sentinel-1 Ground Range Detected (GRD) data and (2) red, green, blue and the near infra-red (NIR) band from Sentinel-2 Bottom-Of-Atmosphere (BOA) reflectance data. We approximate building groups in an interested region as a combination of numerous cuboids whose bottom areas equal resolution of used building height data set (10 m×10 m or 100 m×100 m) and heights equal building heights at corresponding pixels (a pixel is 10 m×10 m or 100 m×100 m). Thus, $A_b$ is the total external surface area of these cuboids per unit ground and can be expressed as:

$$A_b = \frac{\sum_{i=1}^{n}\sum_{j=1}^{m}\left(dH_{-1}^{0}+dH_{1}^{0}+dH_{0}^{-1}+dH_{0}^{1}\right)\chi_r + S_{top}}{n \cdot m \cdot {\chi_r}^2}$$

$$dH_a^b = \max\left(\left(H_{i,j} - H_{i+a,j+b}\right), 0\right) \quad (1)$$

$$S_{top} = \begin{cases} {\chi_r}^2, & H_{i,j} \neq 0 \\ 0, & H_{i,j} = 0 \end{cases}$$

Where i and j are the horizontal position of pixels in an interested region. Symbols n and m characterize the size of the interested region. H is the building height at corresponding pixels. $\chi_r$ is the spatial resolution of building height data (10m or 100m). $S_{top}$ is the top area of buildings.

**Calculation of effective landcover geometric area per unit ground for an observation site**

The key point of calculation effective landcover geometric area per unit ground ($A_L$) for an observation site is to determine the region where landcover geometry can significantly influence observed ADD velocity of the site. An observed ADD velocity of an observation site represent the mean condition of air mass passing through the site within a sampling time interval (30 min in general). The sampled air mass during a sampling time interval includes all air within a certain distance upwind of the site. The certain distance, $L_{air}$, can be expressed as $U_m \cdot \Delta t$, where $U_m$ and $\Delta t$ refer to the mean wind speed and sampling time interval respectively. We use $D_f(x)$ to denote the fraction of deposited aerosols of a sampled air mass within x meter upwind of an observation site to total deposited aerosols of the sampled air mass. Assuming ADD velocity ($V_d$) and aerosols concentration ($C_a$) do not significantly vary within $L_{air}$ upwind of the site, we have:

$$\frac{dD_f}{dx} = \frac{\frac{L_{air}-x}{U_m}V_d C_a}{\int_0^{L_{air}}\frac{L_{air}-x}{U_m}V_d C_a dx} = \frac{2(L_{air}-x)}{{L_{air}}^2} \quad (2)$$

Where $\frac{dD_f}{dx}$ denotes the fraction of deposited aerosols of a sampled air mass within unit distance at the point x meter upwind of an observation site (to total deposited aerosols of the sampled air mass). Equation (2) reveals that landcover near an observation site has larger impact on observed ADD velocity. According to equation (2), $D_f(x)$ can be expressed as:

$$D_f(x) = \frac{2}{{L_{air}}^2}(L_{air}x - \frac{x^2}{2}) \quad (3)$$

According to equation (3), we define the effective radius ($r_{eff}$) of an observation site as 0.29 $L_{air}$, within which deposited aerosols of a sampled air mass contribute to 50% total deposited aerosols (i.e., $D_f$ ($r_{eff}$)=50%). The effective radius for 14 observation sites mentioned in main text ranges from ~300m to ~3000m. Thus, effective $A_L$ for an observation site is defined as averaged $A_L$ within effective radius of the observation site. $A_L$ is the sum of $A_v$, $A_b$, and uncovered soil/water per unit ground. For simplicity, uncovered soil/water per unit ground is set to be 1 $m^2/m^2$. This simplification should introduce small uncertainty as aerosols are mainly trapped by upper part of a canopy (75%~90%)[42].

**Global canopy height and tree density**

Canopy height and tree density are the necessary inputs for our new framework to predict ADD velocity. Canopy height data used in this study are obtained from Satellite-Based Global Land Surface Datasets for Earth System Model Applications (NCEI Accession 0295750, https://www.ncei.noaa.gov). This dataset includes key land surface properties based on various operational satellite measurements (e.g. MODIS, VIIRS and GEDI). They include the land surface type, vegetation clumping index, leaf area index, vegetative canopy height, and green vegetation fraction. Critical processing steps are taken to extend the surface properties for full global coverage, as well as gap-filling. All variables are gridded to universal global latitude/longitude gridded coordinates (-90° - 90° in latitude and 0° - 360° in longitude) with a consistent spatial resolution of 0.01° (~ 1 km). Tree density data used in this work are obtained from Crowther et al. 2015[43]. These data are generated by generalized linear regression models trained by ground-sourced measurements of tree numbers and geographic information systems (GIS) data. Total 429775 ground-sourced measurements are collected from international forestry databases, including the Global Index of Vegetation-Plot Database (GIVD http://www.givd.info), the Smithsonian Tropical Research Institute (http://www.stri.si.edu), ICP-Level-I plot data which cover most of Europe (http://www.icp-forests.org), and National Forest Inventory (NFI) analyses from 21 countries, including the USA (http://fia.fs.fed.us/) and Canada (https://nfi.nfis.org/index.php). The GIS data for developing predictive regression models are derived through satellite-based remote sensing and ground-based weather stations, and can be loosely grouped into four categories: topographic, climatic, vegetative or anthropogenic. Topographic covariates include elevation, slope, aspect (as northness and eastness), latitude (as absolute value of latitude) and terrain roughness index (TRI). Climatic covariates include annual mean temperature, temperature annual range, annual precipitation, precipitation of driest month, precipitation seasonality (coefficient of variation), precipitation of driest quarter, potential evapotranspiration per hectare per year, and indexed annual aridity. Vegetative covariates include, enhanced vegetation index (EVI), leaf area index (LAI), dissimilarity, contrast, and angular second moment. anthropogenic covariate is proportion of urban and/or developed land cover. Predictive regression models are separately generated for the forested areas in each of the 14 biomes as defined by The Nature Conservancy (http://www.nature.org).

Spatial resolution of this data set is 0.01° (~ 1 km).

**Atmospheric aerosol flux observations**

We introduce the principle of atmospheric aerosol flux observations first. In the view of Reynolds Averaging, vertical fluxes of aerosols ($F_a$) can be expressed as:

$$F_a = \overline{w'C_a{}'} = \frac{1}{n}\sum_{i=1}^{n}(w_i - \overline{w})\left(C_a^i - \overline{C_a}\right) \quad (4)$$

Where w is the vertical component of wind. $C_a$ is the aerosol concentration. Thus, one can measure $F_a$ at single site with high frequency wind data and aerosol concentration data, which is named eddy covariance technique (EC). The high frequency wind data are usually measured by an ultrasonic anemometer, while the high frequency particle concentration data are generally measured by a condensation particle counter (CPC) or a fast mobility particle sizer (FMPS). Negative $F_a$ refers to deposition and positive $F_a$ refers to emissions. In case of negative $F_a$, ADD velocity is expressed as $F_a/\overline{C_a}$. ADD velocity can be calculated over varying timescales, but 30 min is typically used in published measurements.

During the past half century, published atmospheric aerosol flux measurements mainly focused on deposition over vegetated regions, with several studies measuring ADD over water. All studies over water[9,44] and studies over vegetated region with available landcover geometry data (i.e., leaf area index)[6,8,12,42,45-53] are chosen either for presenting the "area law" in main text or validating proposed ADD framework. However, there is still no atmospheric aerosol flux measurement over built-up regions so far.

To fill this gap, we conduct the first atmospheric aerosol flux measurement over a Chinese megacity, Guang Zhou, during 2024/9/27/-2024/11/10. The observation site is selected at 23 floors (118m) of Guangzhou Tower (total 600 m, 23°6′N, 113°18′E) in Haizhu district, a highly developed region in Guang Zhou, to ensure ~twice the height of surrounding buildings (~50m). In this observation campaign, three-dimensional high-frequency (20 Hz) windspeed data were collected by a Gill WindMaster ultrasonic anemometer. Aerosol size distributions were measured by a SMPS consisting of a soft X-ray neutralizer (TSI Inc., model 3088), a differential mobility analyzer (DMA, TSI Inc., model 3081A) and an ultrafine condensation particle counter (UCPC, TSI Inc., model 3756) with time resolution of 5 minutes. High frequency data (10 HZ) about the concentration of aerosols larger than ~6nm were measured by another condensation particle counter (CPC, TSI Inc., model 3750). Time scale for flux calculation is 30 minutes.

To derive size-resolved aerosol fluxes, we designed two sampling lines. During 2024/9/27-2024/11/1, the first sampling line was made of a ~10m length and 1/4 in. outer diameter Teflon tube with flow rate of ~2.5 L $min^{-1}$. The sample line was separated into 2 paths ~10cm away from CPC/SMPS, with one path of 1.5 L $min^{-1}$ flow rate for SMPS and another path of 1 L $min^{-1}$ flow rate for CPC. A Nafion dryer (Perma Pure, MD-700−24F-3) was set in front of CPC/SMPS to ensure <40% relative humidity (RH) during sampling. The aerosol residence time in this sample line was estimated as ~10s. Size-resolved aerosol fluxes were obtained by matching geometric

mean diameters of measured mean aerosol size distributions during 30 minutes to measured aerosol fluxes. According to Pryor et al. 2007[50], this approximation is only valid for unimodal aerosol size distributions. The measured geometric mean diameters ranged from ~20 nm to ~100 nm during this period. Thus, we need obtain aerosol fluxes of larger size through another way. During 2024/11/2-2024/11/10, the second sampling line was made of a ~10m length and 1/4 in. outer diameter Teflon tube with flow rate of ~1.5 L $min^{-1}$ and was only linked to SMPS. A Nafion dryer is also used to keep RH below 40%. In this period, we keep constant DMA voltage to get high frequency aerosol concentration at single bin (98~102 nm, 194~202 nm, 299~311 nm, 399~414 nm and 478~496 nm), which can be directly used to calculate size-resolved aerosol fluxes. Aerosol residence time in this sample line was estimated as ~10s.

We ensure quality of the final aerosol flux data by conducting three necessary steps: timelag correction, spectral analysis and uncertainty estimation. A timelag of ~10 s was considered when we matched high frequency aerosol concentration data to high-frequency windspeed data for calculating aerosol fluxes. The timelag stemmed from ~10 s distance for sampled flow between the ultrasonic anemometer and SMPS/CPC. Because aerosol fluxes are dominantly contributed by energy-containing range and inertial subrange of turbulence, measured covariance of vertical wind and aerosol concentration should cover the two ranges. This can be tested by spectral analysis. Two example cospectra in 2024/10/25 (Supplementary Fig. S6a) and 2024/11/4 (Supplementary Fig. S6b) represent abovementioned two measurement period. Characteristic inertial subrange ($f^{-4/3}$) predicted by Kolmogorov theory or Kaimal's empirical model[54] is observed at 1.2~14 Hz (i.e., f=72~840) for the first period and 3~20 (i.e., f=180~ 1200) Hz for the second period, which demonstrates a sufficient frequency range of measured covariances. Although multiple reasons will lead to uncertainty of EC technique, we only consider three well-understanded uncertainty sources of measured aerosol fluxes, namely instrument uncertainty, sampling uncertainty and electronic noises. Reported instrument uncertainties of ultrasonic anemometer and SMPS/CPC is ~3% and 10% respectively. Thus, overall instrument uncertainty is estimated as 10% during this campaign. Sampling uncertainty is caused by the fact that limited samples collected for calculating fluxes cannot characterize overall flux of a large region. According to the method proposed by Finkelstein et al. 2001[55], sampling uncertainty in this study was estimated as 25%. Electronic noises are significant influenced by the environment where the instruments are running. For EC technique, electronic noises can be calculated by differences between theoretical cospectrums and measured cospectrums at high frequency region. Estimated electronic noise in this study is less than 1%. Thus, the total uncertainty for measured aerosol fluxes is ~35%.

**Controlled aerosol deposition experiments in a laboratory**

Characterizing ADD in a laboratory at controlled conditions provides a perfect way to investigate influences of single variable on this process. Laboratory studies about ADD are usually conducted in a duct. Measured ADD velocities ($V_d$) can be calculated by aerosol penetration (p), the ratio of aerosol concentration at the duct outlet to that at the duct inlet. Measured $V_d$ characterizes deposition at all parts of a duct (ceiling, ground and walls). As gravity-induced suppression for aerosol deposition at ceiling is expected to offset gravity-induced enhancement for aerosol deposition at ground, the measured $V_d$ is only caused by air-aerosol collision. Several studies

measuring ADD velocity through fluorescent techniques are also included in our analysis, with experimental details presented elsewhere[19,56]. The reported deposition experiments[19,20,56-66] are summarized in Extended Data Fig. 2-4 and Supplementary Table 2. To the best of our knowledge, all published laboratory studies of ADD over the past half century in which ADD velocity was measured were included. Most experiments were conducted in ducts made of single smooth material (e.g., glass, wax coated, or metals), whose micro roughness typically ranges from 0.5 to 5 μm according to reported measurements for these materials[67-71] (https://www.alleima.ph/en/products/strip-steel/surfaces/; https://www.raychemrpg.com/customised/build-to-print/sheet-metal-fabrication). Only two study[19,20] reported ADD velocity over different surfaces made of glass, roughened brass or diverse sandpapers (measured micro roughness of 70, 100, 150, and 250 μm). Friction velocity in most reported experiments was not directly measured but was estimated based on different empirical methods. Thus, for comparability and consistency of these reported data, we recalculated friction velocity in these experiments by a unified classic method from Liu et al. (1974)[60] and White et al. (1986)[72]:

$$u^* = \bar{u}\sqrt{\frac{f}{2}}$$
$$\frac{1}{\sqrt{f}} = -3.6\log\left(\frac{6.9}{R_e} + \left(\frac{k}{3.7D_h}\right)\right) \quad (5)$$

Where $u^*$ is the friction velocity. $\bar{u}$ is the mean wind speed in a duct. f is the friction factor. $R_e$ is the Reynolds Number. k is the micro roughness of duct inner surface. $D_h$ is the duct diameter. Equations (5) are obtained from a series of wind tunnel experiments for turbulence. These reported data spanning more than half a century indicate that ADD over canopy-free landcover is significantly influenced by in-situ fiction velocity ($u^*$, Extended Data Fig. 4), aerosol diameter ($D_p$, Extended Data Fig. 3) and landcover micro roughness ($k_L$, Extended Data Fig. 2).

**One-dimensional Eulerian ADD model**

The used ADD model for canopy-free landcover is improved form several published one-dimensional Eulerian ADD models[73-76], which explicitly describe aerosol motion in viscous sublayer and buffer layer driven by different mechanisms. The differences between these published models lie in aerosol motion mechanisms considered and the corresponding expressions. Considered aerosol motion mechanisms in these published models include turbulent entrainment, Brownian motion, gravitational settling and turbophoresis. ADD velocity in viscous sublayer or buffer layer induced by the four mechanisms can be derived from the following aerosol motion equation:

$$J = \left(\varkappa_p + D\right)\frac{\partial C}{\partial y} + V_{tur}C + V_g C \quad (6)$$

Where J is the aerosol flux within viscous sublayer or buffer layer. $\varkappa_p$ is the turbulent diffusion coefficient for aerosols. D is the Brownian diffusion coefficient for particles. $V_{tur}$ is the turbophoresis velocity. $V_g$ is the gravitational settling velocity. y is the distance away from landcover. Landcover micro roughness ($k_L$) influences predicted ADD velocity by changing boundary condition to solve equation (6). In published models, $\varkappa_p$ is derived from experiments or direct numerical simulation (DNS) of Navier-Stokes Equation[77] while D, $V_g$, and $V_{tur}$ are derived from aerosol dynamics[23]. In the steady-state condition (i.e., J is independent of y), the analytical solution of ADD velocity can be derived from equation (6)[74,75].

We make two modifications based on these published models. The first modification is the expression of $V_{tur}$. The expression of $V_{tur}$ used in published models is derived under several untested assumptions[24]. We therefore modify the expression of $V_{tur}$ with recent published numerical simulations of multiphase flow (see Supplementary, equation 71)[78]. The second modification is to add aerosol motion in inertial sublayer. Earth science concerns ADD velocity in inertial sublayer, while original models only predicted ADD velocity within viscous sublayer and buffer layer. We related ADD velocity in inertial sublayer to ADD velocity at the outer edge of buffer layer by (see proof in Supplementary, section 1.1):

$$V_d^{ISL} = V_g + \frac{1}{\frac{\Gamma}{u^*} + \frac{1}{V_d^{BL} - V_g}} \tag{7}$$

Where $V_d^{ISL}$ is the ADD velocity in inertial sublayer. $u^*$ is the in-situ friction velocity. $\Gamma$ is the parameter related to atmospheric thermal condition. $V_d^{BL}$ is the ADD velocity at the outer edge of buffer layer and is obtained by solving equation (6). We define $V_d^{BL} - V_g$ as the third collisional deposition velocity ($V_{tc}$), a concept further used in proposed ADD framework. The two modifications make our improved model agree better with controlled deposition experiments than original models. Although well explaining ADD over canopy-free landcover, existing one-dimensional Eulerian ADD models have never been used to predict ADD in real atmosphere. This should be attributed to the fact that vegetation (i.e., canopies) covers 60-80% of the global land.

**Core mathematical expression of ADD velocity in PWM theory**

The conceptional introduction of proposed ADD framework and detailed mathematical derivation of ADD velocity are provided in main text and Supplementary respectively. Here we only introduce the core mathematical expression of ADD velocity ($V_d$). For canopy-free landcover or a homogenous canopy (a homogenous canopy contains either vegetations or buildings and all vegetations or buildings have the same micro roughness. A heterogenous canopy can be generally divided into several homogeneous canopies), we have:

$$\begin{aligned} V_d &= V_g + V_{fc} \\ V_{fc} &= \frac{1}{\frac{\Gamma}{u^*} + \frac{1}{V_{sc}}} \end{aligned} \tag{8}$$

$$V_{sc} = \left( \frac{V_{tc}^{g,+}\left(1-tanh\left(\frac{\beta}{2}\right)\right)}{1+tanh\left(\frac{\beta}{2}\right)} + \frac{\varepsilon \cdot \xi \cdot A_c \cdot \widetilde{V_{tc}^{c,+}} \cdot tanh\left(\frac{\beta}{2}\right)}{\frac{\beta}{2}\left(1+tanh\left(\frac{\beta}{2}\right)\right)} \right) \cdot u^*$$

$$V_{tc}^{g,+} = V_{tc}^{+}\left(D_p,\ k_{ground},\ e^{-\beta}u^*\right)$$

$$\widetilde{V_{tc}^{c,+}} = V_{tc}^{+}\left(D_p,\ k_{canopy},\ \left(\frac{1-\ e^{-\frac{\beta^2}{2}}}{2\beta^2}\right)u^*\right)$$

$$V_{tc}\left(D_p, k, u^*\right) = V_{tc}^{+}\left(D_p, k, u^*\right) \cdot u^*$$

Where $V_{fc}$ is defined by us as the first collisional deposition velocity which refers to the ADD velocity caused by air-aerosol collisions at an observation site (in inertial sublayer). $V_{sc}$ is defined by us as the second collisional deposition velocity which refers to the ADD velocity caused by air-aerosol collisions at the top of roughness sublayer. $V_{tc}$ is defined by us as the third collisional deposition velocity which refers to the ADD velocity caused by air-aerosol collisions at the outer edge of viscous domain (i.e., the outer edge of buffer layer). Illustration of $V_{fc}$, $V_{sc}$, and $V_{tc}$ is shown in Extended Data Fig. 8. As mentioned before, $\Gamma$ is the parameter related to atmospheric thermal condition. $V_g$ is the gravitational settling velocity. $\beta$ is the wind attenuation coefficient which characterizes the suppression of wind by a canopy. $\varepsilon$ is the enrichment coefficient which characterizes aerosol enrichment degree at external surface of canopy structures (e.g., leaf external surface or building external surface). $\xi$ is the effective area correction coefficient which characterizes the sheltering effect of outer leaves on inner leaves. $A_c$ is the canopy geometry area per unit ground (For homogeneous canopy, $A_c$=$A_v$ or $A_b$). $u^*$ is the in-situ friction velocity. $D_p$ is the aerosol diameter. $k_{ground}$ and $k_{canopy}$ are the micro roughness for ground and external surface of canopy structures respectively. $V_{tc}^{g,+}$ and $\widetilde{V_{tc}^{c,+}}$ are the dimensionless third collisional deposition velocity for ground and canopies. All these parameters are theoretically or experimentally determined and are detailed in Supplementary, section 1.4. When $A_c$=0, the proposed framework is simplified to the form of mentioned one-dimensional Eulerian ADD models for canopy-free landcover (Supplementary, equation 67 and the following text). Thus, our framework is able to predict ADD velocity over landcover with any geometry. In addition, although more complicated than resistance model, ADD velocity in the new framework is still explicitly formulated. According to our test in CESM, the proposed framework barely increases computational cost compared to resistance model. As a result, the substantial improvement in ADD prediction (especially the first established connection between ADD and landcover geometry), achieved without increasing computational cost, makes our new ADD framework a better choice than resistance model for next-generation Earth-system models.

**Scale analysis of aerosol motion**

To derive an explicit expression of ADD velocity, simplifying aerosol motion equations based on scale analysis is necessary. Air entrainment (advection entrainment and turbulent entrainment),

turbophresis, Brownian motion, and gravitational settling are the four mechanisms driving aerosol deposition. We characterize the four mechanisms by five characteristic time scales (air entrainment are characterized by two time scales) respectively: advection entrainment drift time ($\tau_{ae}$), turbulent entrainment drift time ($\tau_{te}$), Brownian drift time ($\tau_b$), gravitational drift time ($\tau_g$), and turbophoresis drift time ($\tau_{tur}$). $\tau_{ae}$, $\tau_{te}$, $\tau_b$, $\tau_g$, and $\tau_{tur}$ are defined as the times required for the corresponding mechanisms (advection entrainment, turbulent entrainment, Brownian motion, gravitational settling and turbophresis) to drive aerosols to move one meter. $\tau_{ae}$, $\tau_{te}$, $\tau_b$, $\tau_g$, and $\tau_{tur}$ are expressed as $\frac{1m}{\widetilde{u^n}}$, $\frac{(1m)^2}{\widetilde{K_p}}$, $\frac{(1m)^2}{D}$, $\frac{1m}{V_g}$, and $\frac{1m}{V_{tur}}$. $\widetilde{u^n}$ is the component of mean wind speed toward landcover external surface in inertial sublayer, drag domain, or viscous domain. $\widetilde{K_p}$ is the aerosol turbulent diffusion coefficient in inertial sublayer, drag domain, or viscous domain, which is approximated as momentum turbulent diffusion coefficient $\widetilde{K_m}$. D is the Brownian diffusion coefficient for aerosols. $V_g$ is the gravitational settling velocity. $V_{tur}$ is the turbophoresis velocity. The scale analysis of aerosol motion based on the five characteristic time scales under typical surface layer conditions is presented in Extended Data Fig. 5 (typical surface layer conditions are detailed in Supplementary Table 1). The larger the time scale, the less important the corresponding mechanism. Thus, Brownian motion, turbophoresis, gravitational settling, and turbulent entrainment dominate aerosol migration in viscous domain (Extended Data Fig. 5a); Gravitational settling, turbulent entrainment, and advection entrainment dominate aerosol migration in drag domain (Extended Data Fig. 5b); Turbulent entrainment and gravitational settling dominate aerosol migration in inertial sublayer (Extended Data Fig. 5c).

**Simulations of global aerosol loading and aerosol forcing**

A new ADD module based on proposed ADD physical framework are developed and coupled into Community Atmospheric Model Version 6 (CAM6). The mathematical form of the new ADD module is provided in Supplementary, section 1.4. Compared to traditional ADD module, additional inputs of landcover data including vegetation geometric area per unit ground ($A_v$), building geometric area per unit ground ($A_b$), building height, vegetation height, and tree density are necessary for our new module. The needed landcover data are read in the new module from outside the CAM, with their sources presented in previous sections. Considering that total urban area only accounts for <1% continental aera, $A_b$ is set to 0.8 $m^2$ $m^{-2}$ for each urban region for simplicity. The dimensionless third collisional deposition velocity ($V_{tc}^+$) required for the new module is also read outside the CAM from a look-up table, which is calculated based on equation (81) in Supplementary, section 1.4. The new ADD module and the corresponding coupling file in Fortran version are provided in Zenodo (https://zenodo.org/records/21807286). Global simulations with the new ADD module and conventional modules (i.e., resistance model with conventional and refitted parameters) are conducted respectively, to evaluate influence of landcover geometry on global climate. All simulations are configured with a spatial resolution of 1.9° × 2.5° for the latitude and longitude grid and 32 hybrid pressure levels and are conducted for the period during 2018-2020.

CAM6 used in our simulation was released by NCAR as the atmospheric component of the

Community Earth System Model (CESM) version 2 with the CMIP6-based emissions for aerosol and precursor gases[21]. A new 4-mode modal aerosol module (MAM4) in CAM6 categorizes various aerosols into four modes: the Aitken mode, accumulation mode, coarse mode, and primary carbon mode. MAM4 contains six chemical components (sulfate, secondary organic matter, sea salt, primary organic matter, BC and dust) and simulate the mass concentration of each component and the number concentration of each mode. Regarding aerosol mixing states, CAM6 assumes internal mixing within modes and external mixing between modes. The size distribution is represented by a lognormal distribution within each mode, with sizes ranging from 0.015 μm to 0.053 μm (Aitken mode), 0.058 μm to 0.48 μm (accumulation mode), 0.4 μm to 40 μm (coarse mode), and 0.06 μm to 0.3 μm (primary carbon mode)[79,80]. The shortwave radiative transfer calculation is provided by the Rapid Radiative Transfer Model for General circulation models (RRTMG)[81]. In the radiative module, the AOD, SSA and asymmetry factor are the parameters that determine the aerosol radiative properties. The solar spectrum is divided into 14 wave intervals from 0.2 to 12.2 micrometers.

**Introduction of the resistance model**

The semi-empirical expression of ADD velocity ($V_d$) in the resistance model is[10]:

$$
\begin{aligned}
V_d &= V_g + \frac{1}{R_a + R_s} \\
R_s &= \frac{1}{\varepsilon_0 u^* (E_b + E_{im} + E_{in})} \\
E_b &= p_1 {S_c}^{p_2} \\
E_{im} &= p_3 \left(\frac{S_t}{p_4 + S_t}\right)^{p_5} \\
E_{in} &= p_6 \left(\frac{D_p}{p_7}\right)^{p_8}
\end{aligned}
\tag{9}
$$

Where $V_g$ is the gravitational settling velocity. $R_a$ is the atmospheric resistance. $R_s$ is the surface resistance. Although $V_g$ and $R_a$ are derived from aerosol dynamics and Monin-Obukhov similarity theory, $R_s$ generally dominates $V_d$ and is completely determined by empirical methods. The mathematical expression of $R_s$ is proposed by analogizing empirical formulas of filter capture efficiency. $E_b$, $E_{im}$ and $E_{in}$ are aerosol empirical loss efficiency in filters induced by Brownian motion, impaction and interception. It should be noticed that Brownian motion, impaction and interception in the context of a filter are defined based on streamlines which means laminar flow[82]. Thus, such analogy is improper for real atmosphere where turbulence generally exists. Eight free parameters in $R_s$, $p_1$-$p_8$, can only be obtained by fitting observed ADD velocity. One may notice the similarity between the most external $V_d$ expressions of PWM theory and the resistance model. This is because they both explicitly describe aerosol motion in inertial sublayer. However, aerosol motion within roughness sublayer generally dominates the whole ADD process. Failing to clarify aerosol motion in the most important ADD phase, resistance model had to empirically and ambiguously express this ADD phase with $R_s$. In contrast, our new framework fundamentally

elucidates aerosol motion within roughness sublayer according to aerosol dynamics and multi-scale fluid dynamics. Therefore, resistance model can be regarded as a highly empirical simplification of PWM theory.

**Data availability**

Core data supporting this paper are available on Zenodo at https://zenodo.org/records/21807286.

**Code availability**

Core codes supporting this paper are available on Zenodo at https://zenodo.org/records/21807286.

**References**


1 Ramanathan, V., Crutzen, P. J., Kiehl, J. T. & Rosenfeld, D. Aerosols, climate, and the hydrological cycle. *science* 294, 2119–2124 (2001).

2 Weis, J. *et al.* One-third of Southern Ocean productivity is supported by dust deposition. *Nature* 629, 603–608 (2024).

3 Gurmesa, G. A. *et al.* Retention of deposited ammonium and nitrate and its impact on the global forest carbon sink. *Nature Communications* 13, 880 (2022).

4 Barkley, A. E. *et al.* African biomass burning is a substantial source of phosphorus deposition to the Amazon, Tropical Atlantic Ocean, and Southern Ocean. *Proceedings of the National Academy of Sciences* 116, 16216–16221 (2019).

5 Farmer, D. K., Boedicker, E. K. & DeBolt, H. M. Dry deposition of atmospheric aerosols: Approaches, observations, and mechanisms. *Annual review of physical chemistry* 72, 375–397 (2021).

6 Petroff, A., Murphy, J. G., Thomas, S. C. & Geddes, J. A. Size-resolved aerosol fluxes above a temperate broadleaf forest. *Atmospheric Environment* 190, 359–375 (2018).

7 Zhang, J., Shao, Y. & Huang, N. Measurements of dust deposition velocity in a wind-tunnel experiment. *Atmospheric Chemistry and Physics* 14, 8869–8882 (2014).

8 Pryor, S. C., Barthelmie, R. J., Spaulding, A. M., Larsen, S. E. & Petroff, A. Size-resolved fluxes of sub-100-nm particles over forests. *Journal of Geophysical Research: Atmospheres* 114 (2009).

9 Caffrey, P. F., Ondov, J. M., Zufall, M. J. & Davidson, C. I. Determination of size-dependent dry particle deposition velocities with multiple intrinsic elemental tracers. *Environmental science & technology* 32, 1615–1622 (1998).

10 Slinn, W. G. N. Predictions for particle deposition to vegetative canopies. *Atmospheric Environment* 16, 1785–1794 (1982).

11 Zhang, L., Gong, S., Padro, J. & Barrie, L. A size-segregated particle dry deposition scheme for an atmospheric aerosol module. *Atmospheric environment* 35, 549–560 (2001).

12 Emerson, E. W. *et al.* Revisiting particle dry deposition and its role in radiative effect estimates. *Proceedings of the National Academy of Sciences* 117, 26076–26082 (2020).

13 Petroff, A. & Zhang, L. Development and validation of a size-resolved particle dry deposition scheme for application in aerosol transport models. *Geoscientific Model Development* 3, 753–769 (2010).

14 Pleim, J. E., Ran, L., Saylor, R. D., Willison, J. & Binkowski, F. S. A new aerosol dry deposition model for air quality and climate modeling. *Journal of advances in modeling earth systems* 14, e2022MS003050 (2022).
15 Blott, S. J. & Pye, K. Particle size scales and classification of sediment types based on particle size distributions: Review and recommended procedures. *Sedimentology* 59, 0037–0746 (2012).
16 Ma, J. *et al.* Effects of leaf surface roughness and contact angle on in vivo measurement of droplet retention. *Agronomy* 12, 2073–4395 (2022).
17 Zhang, Z., Liu, F., Zhou, Z., He, Y. & Fang, H. Roughness measurement of leaf surface based on shape from focus. *Plant methods* 17, 1746–4811 (2021).
18 Seker, D. Z. & Tavil, A. Evaluation of exterior building surface roughness degrees by photogrammetric methods. *Building and Environment* 31, 0360–1323 (1996).
19 Lai, A. C. K. & Nazaroff, W. W. Supermicron particle deposition from turbulent chamber flow onto smooth and rough vertical surfaces. *Atmospheric Environment* 39, 1352–2310 (2005).
20 El, S. Experimental measurements of aerosol deposition to smooth and rough surfaces. *Atmospheric Environment* 17, 639–644 (1983).
21 Danabasoglu, G. *et al.* The community earth system model version 2 (CESM2). *Journal of Advances in Modeling Earth Systems* 12, 1942–2466 (2020).
22 Rasch, P. J. *et al.* An overview of the atmospheric component of the Energy Exascale Earth System Model. *Journal of Advances in Modeling Earth Systems* 11, 1942–2466 (2019).
23 Seinfeld, J. H. & Pandis, S. N. *Atmospheric chemistry and physics: from air pollution to climate change*. (John Wiley & Sons, 2016).
24 Caporaloni, M., Tampieri, F., Trombetti, F. & Vittori, O. Transfer of particles in nonisotropic air turbulence. *Journal of the atmospheric sciences* 32, 565–568 (1975).
25 Stull, R. B. *An introduction to boundary layer meteorology*. (Springer Science & Business Media, 2012).
26 van Donkelaar, A. *et al.* Monthly Global Estimates of Fine Particulate Matter and Their Uncertainty. *Environmental Science & Technology* 55, 15287–15300 (2021). https://doi.org/10.1021/acs.est.1c05309
27 Stevens, C. J., Dise, N. B., Mountford, J. O. & Gowing, D. J. Impact of nitrogen deposition on the species richness of grasslands. *Science* 303, 1876–1879 (2004).
28 Li, X. *et al.* Underappreciated role of canopy nitrogen deposition for forest productivity. *Proceedings of the National Academy of Sciences* 122, e2508925122 (2025).
29 Hautier, Y. *et al.* Anthropogenic environmental changes affect ecosystem stability via biodiversity. *Science* 348, 336–340 (2015).
30 Ghausi, S. A., Zehe, E., Ghosh, S., Tian, Y. & Kleidon, A. Thermodynamically inconsistent extreme precipitation sensitivities across continents driven by cloud-radiative effects. *Nature Communications* 15, 2041–1723 (2024).
31 Ruppert Jr, J. H., Wing, A. A., Tang, X. & Duran, E. L. The critical role of cloud–infrared radiation feedback in tropical cyclone development. *Proceedings of the National Academy of Sciences* 117, 27884–27892 (2020).

32 Girardin, C. A. J. *et al.* Nature-based solutions can help cool the planet—if we act now. *Nature* 593, 191–194 (2021).
33 Pretzsch, H. Canopy space filling and tree crown morphology in mixed-species stands compared with monocultures. *Forest Ecology and Management* 327, 251–264 (2014).
34 Ma, H. & Liang, S. Development of the GLASS 250-m leaf area index product (version 6) from MODIS data using the bidirectional LSTM deep learning model. *Remote sensing of environment* 273, 112985 (2022).
35 Xiao, Z. *et al.* Long-time-series global land surface satellite leaf area index product derived from MODIS and AVHRR surface reflectance. *IEEE Transactions on Geoscience and Remote Sensing* 54, 5301–5318 (2016).
36 Verger, A. *et al.* GEOV2: Improved smoothed and gap filled time series of LAI, FAPAR and FCover 1 km Copernicus Global Land products. *International Journal of Applied Earth Observation and Geoinformation* 123, 103479 (2023).
37 Justice, C. O. *et al.* An overview of MODIS Land data processing and product status. *Remote sensing of Environment* 83, 3–15 (2002).
38 Baret, F. *et al.* LAI, fAPAR and fCover CYCLOPES global products derived from VEGETATION: Part 1: Principles of the algorithm. *Remote sensing of environment* 110, 275–286 (2007).
39 Gonsamo, A. & Chen, J. M. Improved LAI algorithm implementation to MODIS data by incorporating background, topography, and foliage clumping information. *IEEE Transactions on Geoscience and Remote Sensing* 52, 1076–1088 (2013).
40 Wu, W.-B. *et al.* A first Chinese building height estimate at 10 m resolution (CNBH-10 m) using multi-source earth observations and machine learning. *Remote Sensing of Environment* 291, 113578 (2023).
41 Li, R., Sun, T., Ghaffarian, S., Tsamados, M. & Ni, G. GLAMOUR: GLobAl building MOrphology dataset for URban hydroclimate modelling. *Scientific Data* 11, 618 (2024).
42 Grönholm, T. *et al.* Aerosol particle dry deposition to canopy and forest floor measured by two-layer eddy covariance system. *Journal of Geophysical Research: Atmospheres* 114 (2009).
43 Crowther, T. W. *et al.* Mapping tree density at a global scale. *Nature* 525, 201–205 (2015).
44 Zufall, M. J., Davidson, C. I., Caffrey, P. F. & Ondov, J. M. Airborne concentrations and dry deposition fluxes of particulate species to surrogate surfaces deployed in southern Lake Michigan. *Environmental science & technology* 32, 1623–1628 (1998).
45 Deventer, M. J., Held, A., El-Madany, T. S. & Klemm, O. Size-resolved eddy covariance fluxes of nucleation to accumulation mode aerosol particles over a coniferous forest. *Agricultural and Forest Meteorology* 214, 328–340 (2015).
46 Gordon, M. *et al.* Aerosol flux measurements above a mixed forest at Borden, Ontario. *Atmospheric Chemistry and Physics* 11, 6773–6786 (2011).
47 Lavi, A. *et al.* Fluxes of fine particles over a semi-arid pine forest: Possible effects of a complex terrain. *Aerosol Science and Technology* 47, 906–915 (2013).
48 Mammarella, I. *et al.* Long-term aerosol particle flux observations. Part II: Particle size statistics and deposition velocities. *Atmospheric Environment* 45, 3794–3805 (2011).

49 Nemitz, E., Gallagher, M. W., Duyzer, J. H. & Fowler, D. Micrometeorological measurements of particle deposition velocities to moorland vegetation. *Quarterly Journal of the Royal Meteorological Society: A journal of the atmospheric sciences, applied meteorology and physical oceanography* 128, 2281–2300 (2002).

50 Pryor, S. C. *et al.* Particle fluxes over forests: Analyses of flux methods and functional dependencies. *Journal of Geophysical Research: Atmospheres* 112 (2007).

51 Vong, R. J., Vong, I. J., Vickers, D. & Covert, D. S. Size-dependent aerosol deposition velocities during BEARPEX'07. *Atmospheric Chemistry and Physics* 10, 5749–5758 (2010).

52 Gallagher, M. W., Choularton, T. W., Morse, A. P. & Fowler, D. Measurements of the size dependence of cloud droplet deposition at a hill site. *Quarterly Journal of the Royal Meteorological Society* 114, 1291–1303 (1988).

53 Lorenz, R. & Murphy Jr, C. E. Dry deposition of particles to a pine plantation. *Boundary-Layer Meteorology* 46, 355–366 (1989).

54 Kaimal, J. C., Wyngaard, J. C. J., Izumi, Y. & Coté, O. R. Spectral characteristics of surface-layer turbulence. *Quarterly Journal of the Royal Meteorological Society* 98, 563–589 (1972).

55 Finkelstein, P. L. & Sims, P. F. Sampling error in eddy correlation flux measurements. *Journal of Geophysical Research: Atmospheres* 106, 3503–3509 (2001).

56 Sippola, M. R. & Nazaroff, W. W. Experiments measuring particle deposition from fully developed turbulent flow in ventilation ducts. *Aerosol Science and technology* 38, 914–925 (2004).

57 Cheng, Y. S. Wall deposition of radon progeny and particles in a spherical chamber. *Aerosol Science and Technology* 27, 131–146 (1997).

58 Da, G. *et al.* An experimental approach to measure particle deposition in large circular ventilation ducts. *Environmental Science and Pollution Research* 22, 4873–4880 (2015).

59 Lee, K. W. & Gieseke, J. A. Deposition of particles in turbulent pipe flows. *Journal of Aerosol Science* 25, 699–709 (1994).

60 Liu, B. Y. H. & Agarwal, J. K. Experimental observation of aerosol deposition in turbulent flow. *Journal of Aerosol Science* 5, 145–155 (1974).

61 McFarland, A. R., Gong, H., Muyshondt, A., Wente, W. B. & Anand, N. K. Aerosol deposition in bends with turbulent flow. *Environmental science & technology* 31, 3371–3377 (1997).

62 Postma, A. K. STUDIES IN MICROMERITICS. II. THE DEPOSITION OF PARTICLES IN CIRCULAR CONDUITS DUE TO THERMAL GRADIENTS. (General Electric Co. Hanford Atomic Products Operation, Richland, Wash., 1961).

63 Shimada, M., Okuyama, K. & Asai, M. Depostition of submicron aerosol particles in turbulent and transitional flow. *AIChE journal* 39, 17–26 (1993).

64 Sun, K., Lu, L., Jiang, H. & Jin, H. Experimental study of solid particle deposition in 90 ventilated bends of rectangular cross section with turbulent flow. *Aerosol Science and Technology* 47, 115–124 (2013).

65 Wells, A. C. & Chamberlain, A. C. Transport of small particles to vertical surfaces. *British*

*Journal of Applied Physics* 18, 1793–1799 (1967).

66 Wu, Z. & Young, J. B. The deposition of small particles from a turbulent air flow in a curved duct. *International Journal of Multiphase Flow* 44, 34–47 (2012).

67 Kayahan, E., Oktem, H., Hacizade, F., Nasibov, H. & Gundogdu, O. Measurement of surface roughness of metals using binary speckle image analysis. *Tribology International* 43, 307–311 (2010).

68 Pápa, Z., Budai, J., Farkas, B. & Toth, Z. Investigation of surface roughness on etched glass surfaces. *Thin Solid Films* 519, 2903–2906 (2011).

69 Kumar, P., Ahuja, I. S. & Singh, R. Effect of process parameters on surface roughness of hybrid investment casting. *Progress in Additive Manufacturing* 1, 45–53 (2016). https://doi.org/10.1007/s40964-016-0004-9

70 Kumar, A., Gulati, V. & Kumar, P. Effects of Process Parameters on Surface Roughness in Incremental Sheet Forming. *Materials Today: Proceedings* 5, 28026–28032 (2018). https://doi.org/https://doi.org/10.1016/j.matpr.2018.10.043

71 Kumar Khare, S., Agarwal, S. & Srivastava, S. Analysis of Surface Roughness during Turning Operation by Taguchi Method. *Materials Today: Proceedings* 5, 28089–28097 (2018). https://doi.org/https://doi.org/10.1016/j.matpr.2018.10.050

72 White, F. M. *Fluid Mechanics*. (McGraw-Hill New York, 1986).

73 Guha, A. A unified Eulerian theory of turbulent deposition to smooth and rough surfaces. *Journal of Aerosol Science* 28, 1517–1537 (1997).

74 Lai, A. C. K. & Nazaroff, W. W. Modeling indoor particle deposition from turbulent flow onto smooth surfaces. *Journal of aerosol science* 31, 463–476 (2000).

75 Zhao, B. & Wu, J. Modeling particle deposition from fully developed turbulent flow in ventilation duct. *Atmospheric Environment* 40, 457–466 (2006).

76 Johansen, S. T. The deposition of particles on vertical walls. *International Journal of Multiphase Flow* 17, 355–376 (1991).

77 Kim, J., Moin, P. & Moser, R. Turbulence statistics in fully developed channel flow at low Reynolds number. *Journal of fluid mechanics* 177, 133–166 (1987).

78 Soldati, A. & Marchioli, C. Physics and modelling of turbulent particle deposition and entrainment: Review of a systematic study. *International Journal of Multiphase Flow* 35, 827–839 (2009).

79 Liu, X. *et al.* Description and evaluation of a new four-mode version of the Modal Aerosol Module (MAM4) within version 5.3 of the Community Atmosphere Model. *Geoscientific Model Development* 9, 505–522 (2016).

80 Liu, X. *et al.* Toward a minimal representation of aerosols in climate models: Description and evaluation in the Community Atmosphere Model CAM5. *Geoscientific Model Development* 5, 709–739 (2012).

81 Mlawer, E. J., Taubman, S. J., Brown, P. D., Iacono, M. J. & Clough, S. A. Radiative transfer for inhomogeneous atmospheres: RRTM, a validated correlated-k model for the longwave. *Journal of Geophysical Research: Atmospheres* 102, 16663–16682 (1997).

82 Hinds, W. C. & Zhu, Y. *Aerosol technology: properties, behavior, and measurement of airborne particles*. (John Wiley & Sons, 2022).

**Acknowledgments**
We thank all scientists, researchers, and staff who contributed to the open-source data used in this work including observations of landcover geometry, ADD velocity and meteorological variables. This work is supported by National Natural Science Foundation of China under grant nos. 22536004 and 22327806. The authors used Deepseek to polish the language of this manuscript. The authors verified the accuracy of all Deepseek outputs.

**Author contributions**
J.G. and J.J conceived and designed the study. J.G. developed phase-wise migration theory, conducted the measurements, collected and organized all the open-source data. J.G. and J.W. developed the new deposition module for CESM. J.W., G.C. and J.G. supported the global simulation. X.Z. checked all the data. J.G. wrote this paper. J.J., J.W., X.Z., R.C., D.W., S.Z., S.M., Y.C., H.Y., H.W., M.W., and T.G. discussed the results and revised the manuscript.

**Competing interests:** The authors declare that they have no competing interests.

Supplementary Information is available for this paper.
Correspondence and requests for materials should be addressed to Jingkun Jiang, jiangjk@tsinghua.edu.cn; Jiandong Wang, jiandong.wang@nuist.edu.cn.
Reprints and permissions information is available at www.nature.com/reprints.

Main Figures

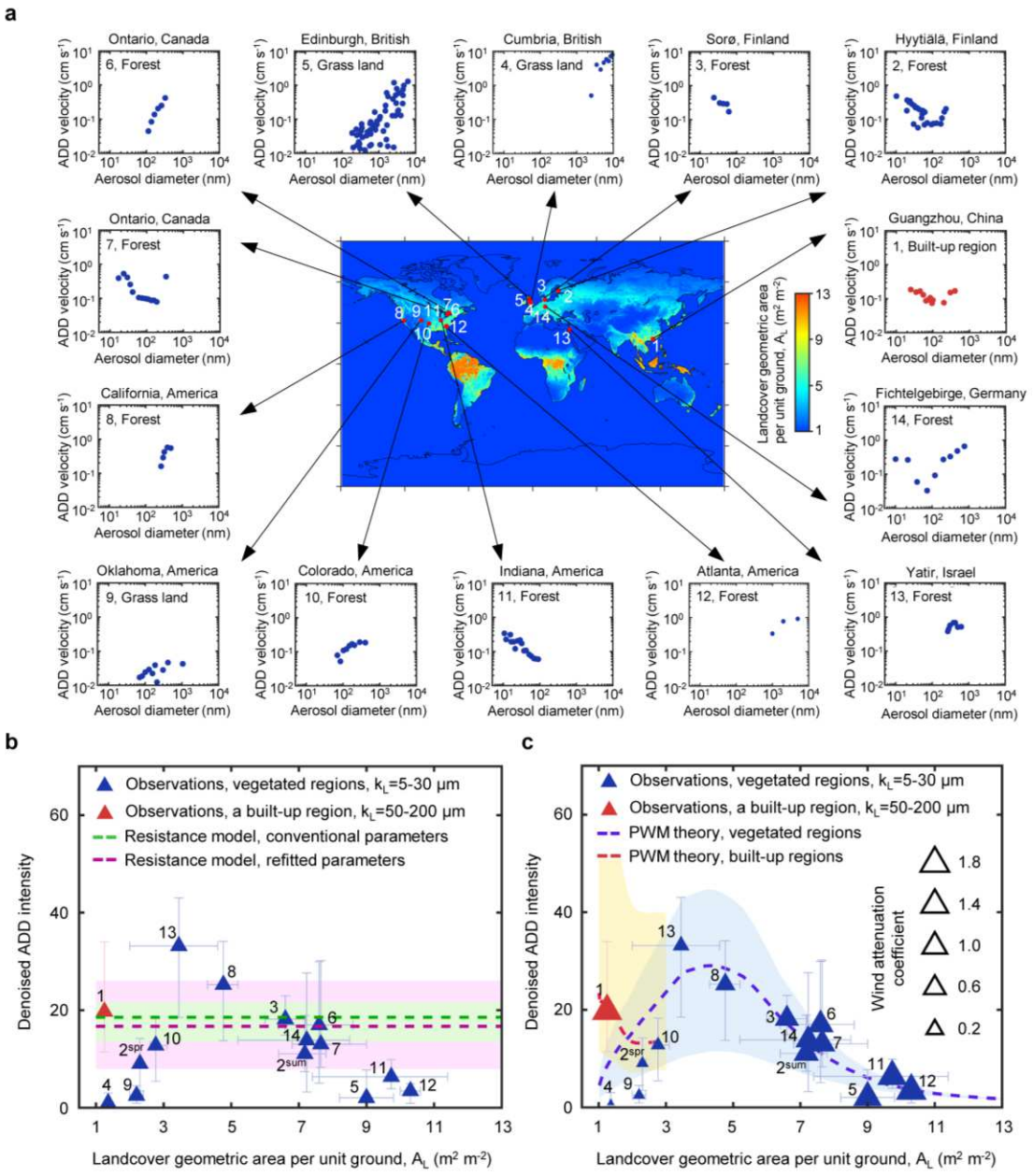



**Fig. 1| The relationship between ADD and landcover geometry. a**, Global observations of ADD velocities. Our measurements over a built-up region are presented in panel 1 as red circles, while published measurements over different vegetated regions are presented in rest panels as blue circles. **b**, The observed and resistance-model-predicted relationships between denoised ADD intensity and landcover geometry. $A_L$ is calculated based on five remote sensing data sets and ground observations (Methods). The red triangle refers to the observed denoised ADD intensity of the built-up region and the blue triangles refer to the observed denoised ADD intensity of different vegetated regions. The vertical error bars of triangles reflect variation of observed ADD velocity in **a**. The horizontal error bars of triangles refer to $A_L$ uncertainty caused by different data sets used

for calculating the parameter. The pink and green dashed lines are the resistance-model-predicted denoised ADD intensity with refitted and conventional parameters respectively. Shaded areas indicate the uncertainties introduced by different land use categories in the resistance model. **c**, The observed and PWM-theory-predicted relationships between denoised ADD intensity and landcover geometry. Triangles and error bars have the same meaning as in **b**. Size of a triangle refers to the wind attenuation coefficient of the corresponding landcover. The blue and yellow shaded areas are the theoretical ranges of denoised ADD intensity predicted by PWM theory for vegetated regions (with $k_L$ ranging from 5 to 30 μm, a typical value for leaves) and built-up regions (with $k_L$ ranging from 50 to 200 μm, a typical value for building exterior wall tiles). The red and blue dashed lines indicate the optimal predictions for built-up regions ($k_L$=80 μm) and vegetated regions ($k_L$=13 μm).

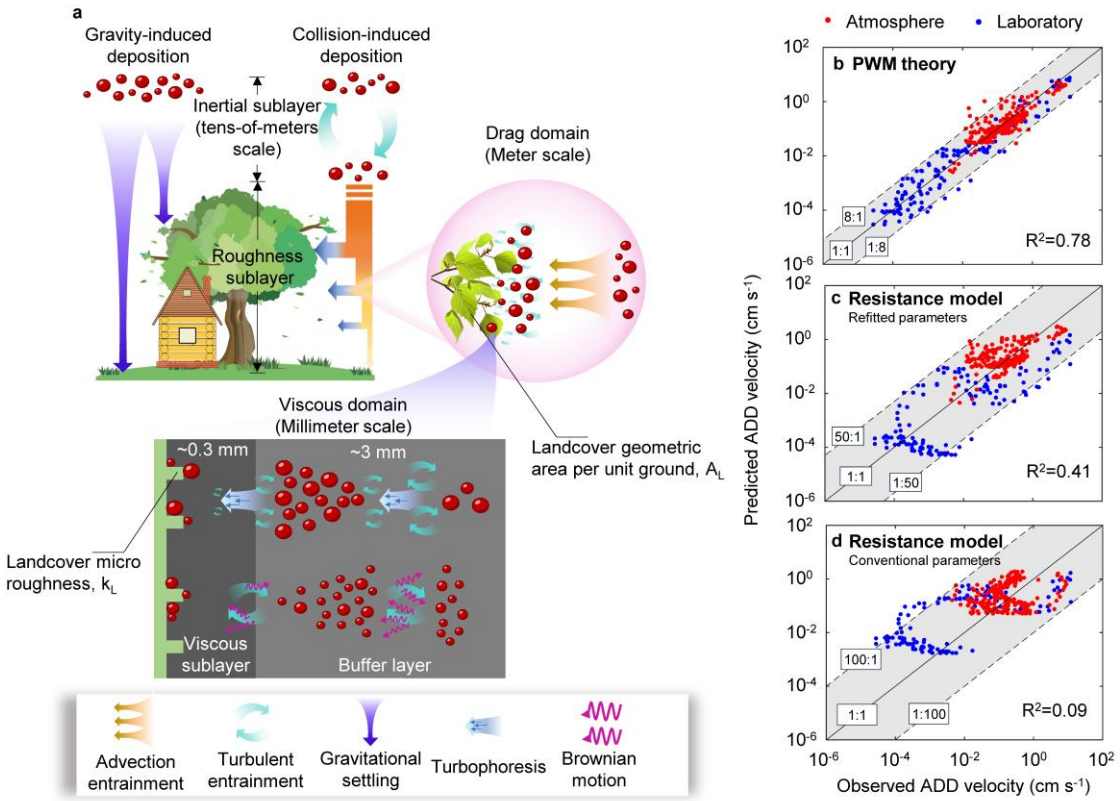



**Fig. 2| Illustration and performance of the new ADD physical framework. a**, Phase-wise migration of aerosols during dry deposition. The whole ADD includes aerosol migrations in inertial sublayer, drag domain (if canopies exist), and viscous domain. Aerosol migrations are driven by gravitational settling, air entrainment (turbulence & advection), Brownian motion, and turbophoresis. Macro landcover geometry (mainly referring to $A_L$) influences aerosol migrations in drag domain and viscous domain by modulating atmospheric motion and the number of aerosol trapping sites within canopy, while micro landcover geometry (i.e., $k_L$) affects the aerosol migration in viscous domain by changing positions of aerosol trapping sites. **b**, Comparison between ADD velocity from observations and the new ADD framework. **c**, Comparison between ADD velocity from observations and the resistance model with refitted parameters. **d**, Comparison between ADD velocity from observations and the resistance model with conventional parameters. Red and blue dots in **b**, **c** and **d** indicate observations from atmospheric flux measurements and controlled laboratory deposition experiments respectively. The grey shaded area covers 95% points.

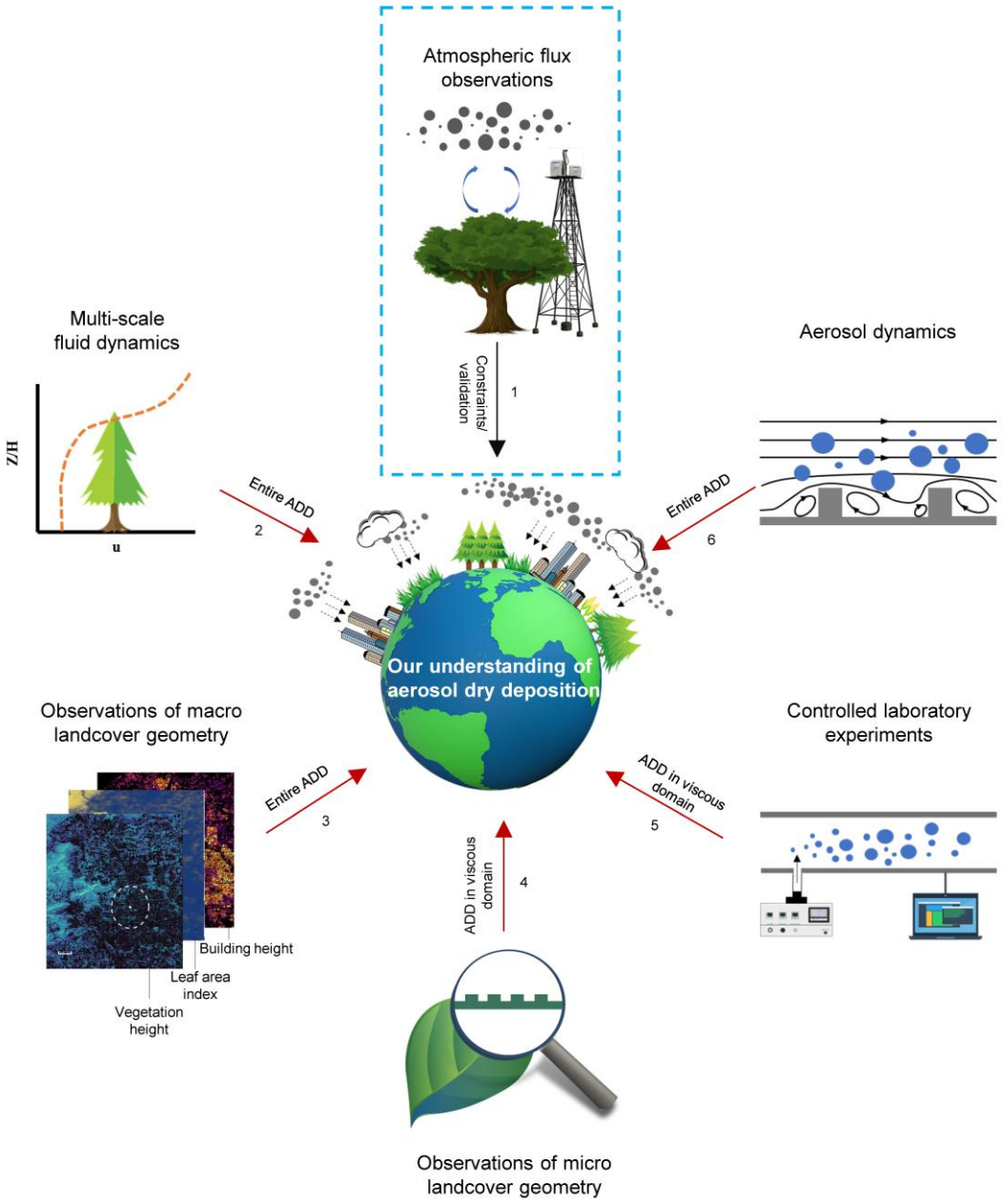



**Fig. 3| Different paths to understand ADD in the new ADD framework.** According to the new framework, progresses in understanding ADD comes from six paths: advances in atmospheric flux observations, muti-scale fluid dynamics, observations of macro landcover geometry, observations of micro landcover geometry, controlled laboratory deposition experiments, and aerosol dynamics. In contrast, progresses in understanding ADD can only come from the advance in atmospheric flux observations under current paradigm supported by the resistance model (the blue box).

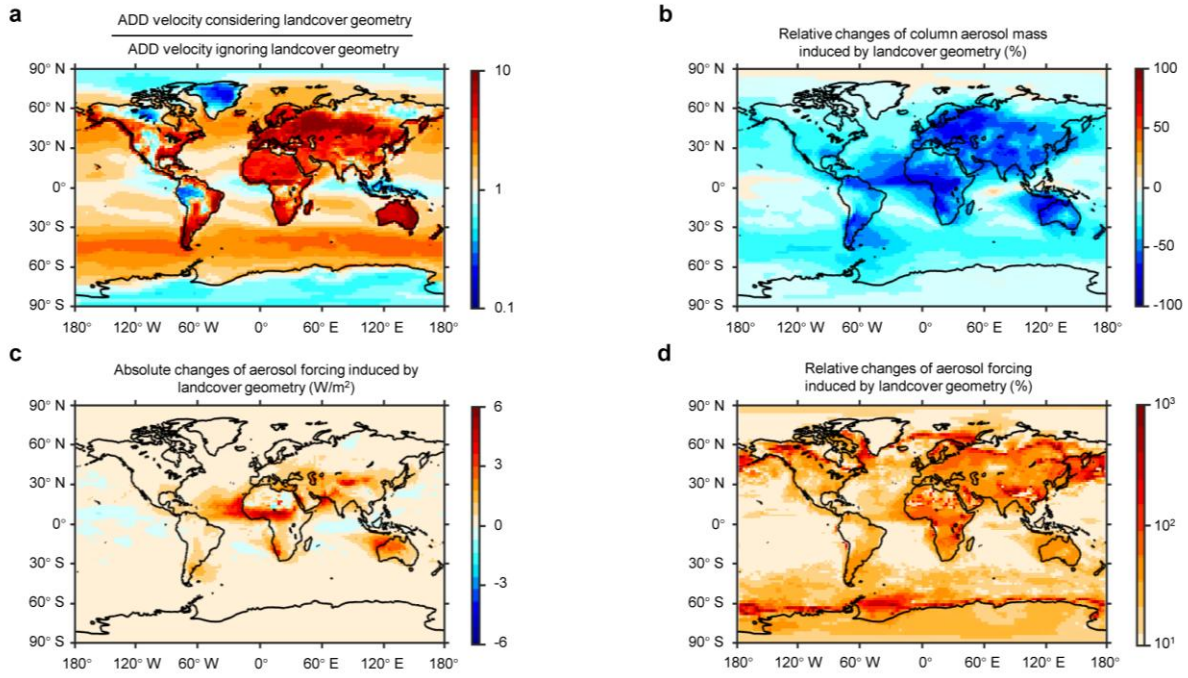


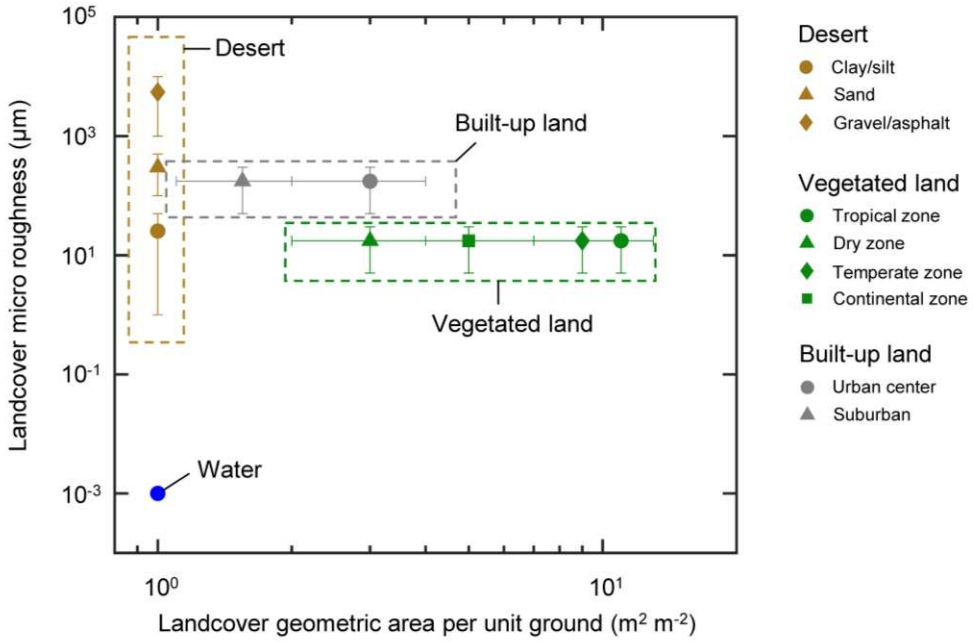

**Fig. 4| Multiple influence of landcover geometry. a**, Influence of landcover geometry on global ADD velocity. **b**, Relative changes of global column aerosol mass induced by landcover geometry (%). **c**, Absolute changes of global aerosol forcing induced by landcover geometry ($W/m^2$). **d**, Relative changes of global aerosol forcing induced by landcover geometry (%).

**Extended Data Table 1|** Description and determination of parameters in PWM theory. More detailed expressions and derivation of these parameters are provided in Supplementary.

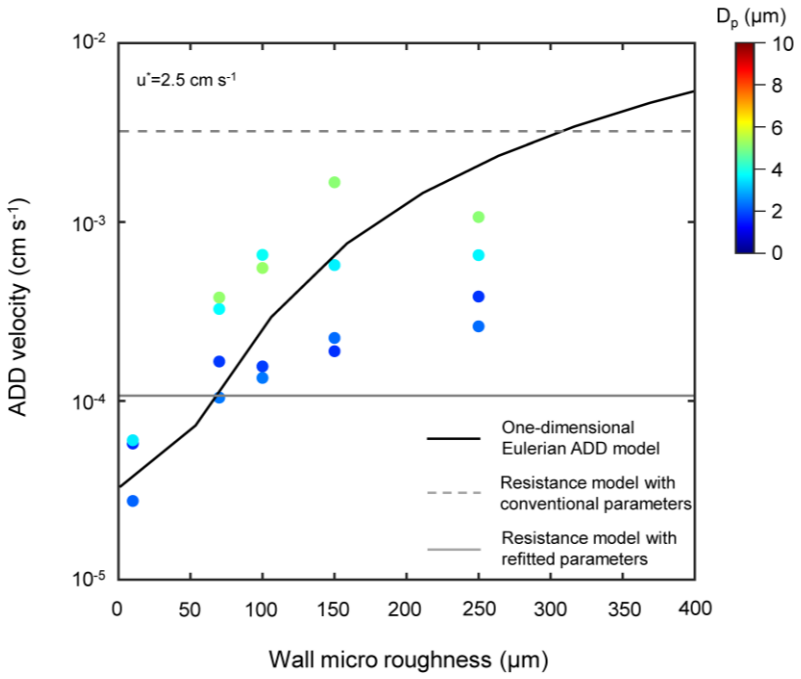
| Parameters | Description | Determination |
|---|---|---|
| $u^*$ | Friction velocity in inertial sublayer | Obtained from in-situ measurements or theoretical calculation from ESM[a] |
| $D_p$ | Aerosol diameter | Obtained from in-situ measurements or theoretical calculation from ESM[a] |
| $k_{ground}/k_{canopy}$ | Surface micro roughness of ground/a canopy | Obtained from in-situ measurements or published measurement reports of different materials |
| $A_c$($A_v$ or $A_b$) | Canopy (vegetation or building) geometric area per unit ground | Obtained from in-situ measurements, remote sensing, or theoretical calculation from ESM[a] |
| $\Gamma$ | A parameter characterizing atmospheric thermal condition | Theoretically derived from Monin-Obukhov similarity theory |
| $\beta$ | Wind attenuation coefficient, characterizing the ability of a canopy to suppress in-canopy atmospheric motion | Derived from canopy meteorology and measured wind profiles in different forests and wind tunnel experiments |
| $\varepsilon$ | Enrichment coefficient, characterizing aerosol enrichment degree at external surface of canopy structures | Theoretically derived from aerosol dynamics and canopy meteorology |
| $\xi$ | Effective area correction coefficient, characterizing the sheltering effect of outer leaves on inner leaves | Theoretically derived from allometry equations |
| Parameters in $V_{tc}^+$ | A series of parameters influencing aerosol motion in viscous domain | Derived from known aerosol dynamics, reported CFD[b] simulations, and reported turbulent structure near wall |

[a] Note: ESM refers to Earth System Model

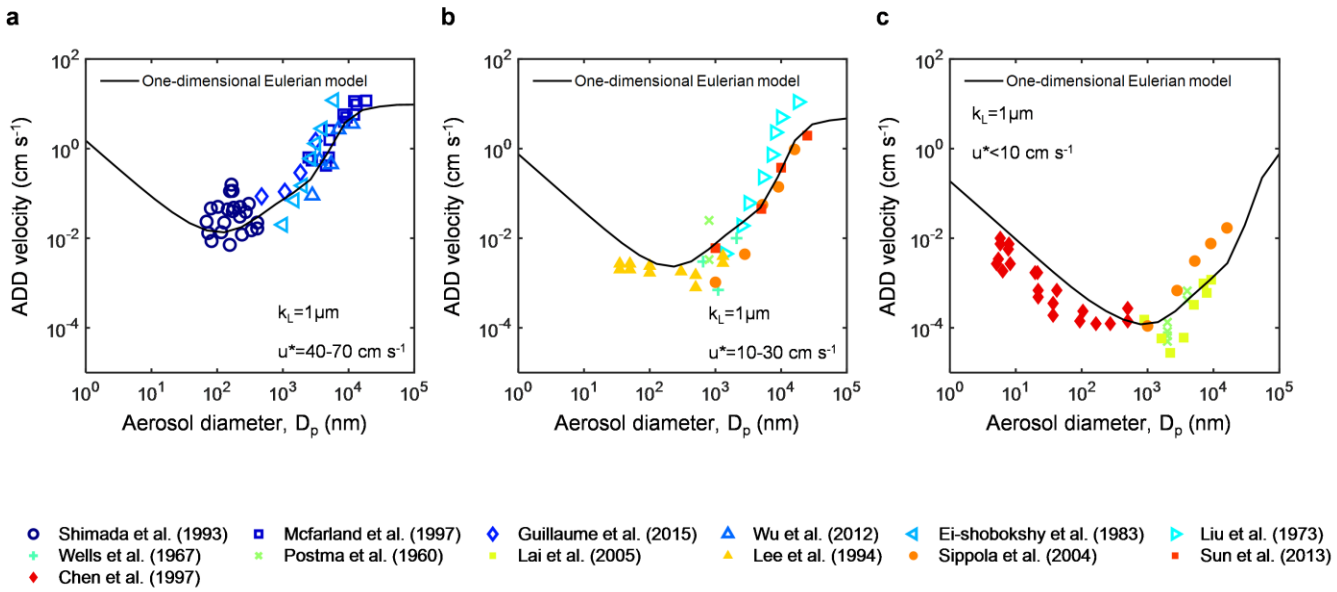
[b] Note: CFD refers to Computational Fluid Dynamics



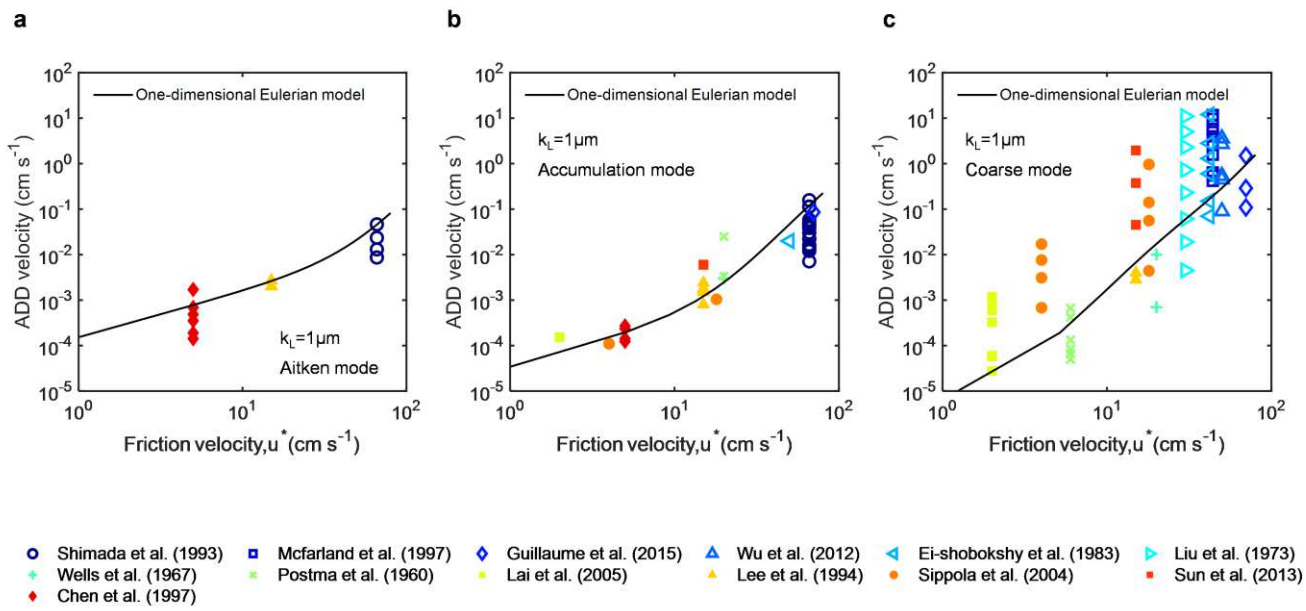

**Extended Data Fig. 1| The geometric characterization for different landcover types.** The blue, brown, grey, and green marks represent water, desert, built-up land and vegetated land respectively. Built-up land only considers buildings. In a geometric view, substantial differences exist both between and within these landcover types.



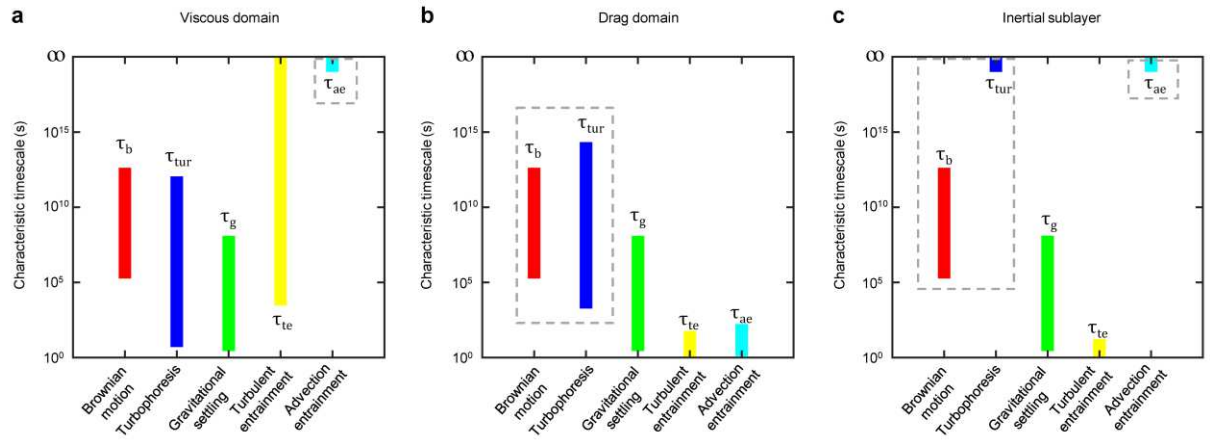

**Extended Data Fig. 2| The dependence of ADD velocity on landcover micro roughness.** The colorful dots are observed ADD velocity in a chamber deposition experiment. Chamber walls adhered with different sandpaper are used to model canopy-free landcover with different micro roughness. In the experiment, aerosols ranging from 1 to 5 μm are selected and friction velocity ($u^*$) is set to ~2.5 cm $s^{-1}$. The black line shows predicted ADD velocity through the one dimensional Eulerian ADD model while grey line and dashed line show modeled ADD velocity through the resistance model with refitted and conventional parameters. Aerosol diameter ($D_p$) is set to 3 μm for all simulations.



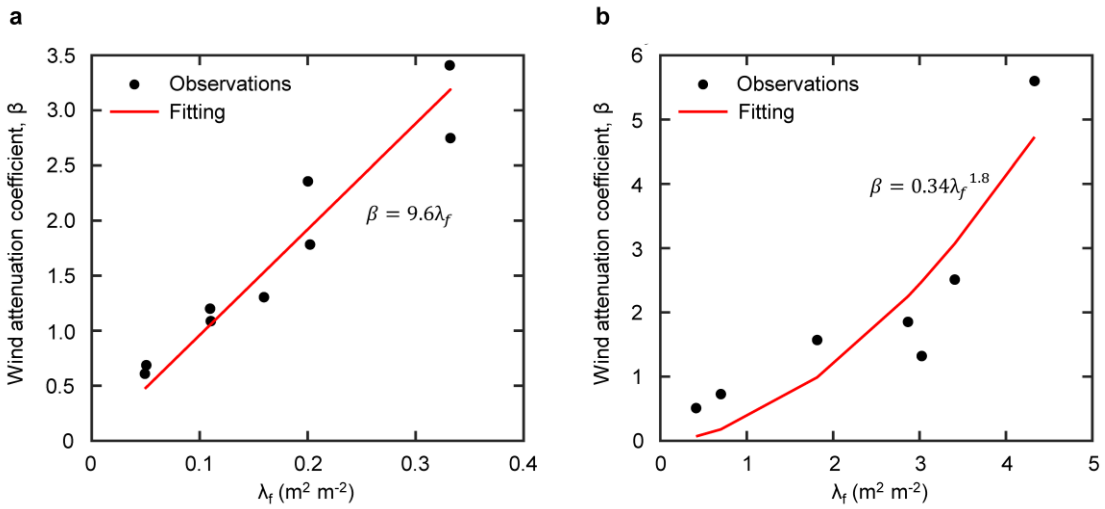

**Extended Data Fig. 3| The dependence of ADD velocity on aerosol diameter. a**, Under strong turbulence condition ($u^*$=40-70 cm $s^{-1}$). **b**, Under moderate turbulence condition ($u^*$=10-30 cm $s^{-1}$). **c**, Under weak turbulence condition ($u^*$=<10 cm $s^{-1}$). Different symbols indicate observed ADD velocity over a smooth surface from published controlled laboratory studies over the past half century. These experiments were mainly conducted in ducts made of metal or glass, whose micro roughness typically ranges from 0.5 to 5 μm according to reported measurements for these materials (Methods). The black lines show predicted ADD velocity by the one dimensional Eulerian ADD model. The wall micro roughness ($k_L$) is set to 1 μm for all simulations. $u^*$ is set to 50, 20, and 5 cm $s^{-1}$ for strong, moderate, and weak turbulence conditions for corresponding simulations.



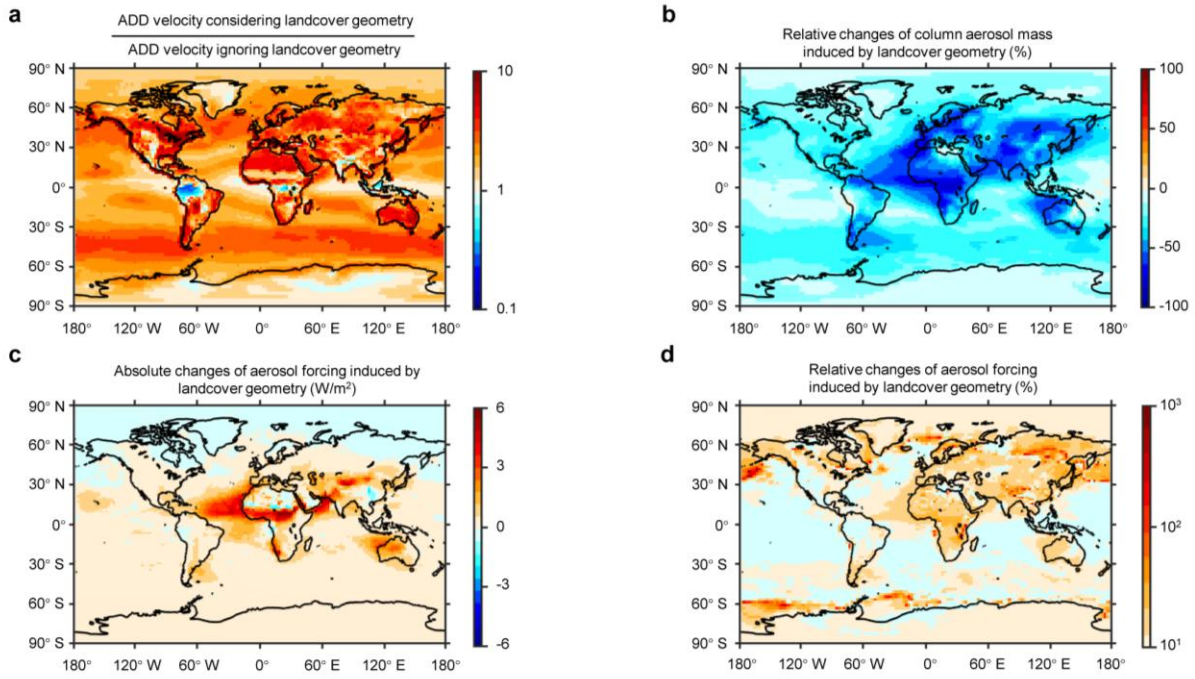

**Extended Data Fig. 4| The dependence of ADD velocity on friction velocity. a**, For Aitken mode. **b**, For accumulation mode. **c**, For coarse mode. Different symbols indicate observed ADD velocity over a smooth surface from published controlled laboratory studies over the past half century. These experiments were mainly conducted in ducts made of metal or glass, whose micro roughness typically ranges from 0.5 to 5 μm according to reported measurements for these materials (Methods). The black lines show predicted ADD velocity by the one dimensional Eulerian ADD model. The wall micro roughness ($k_L$) is set to 1 μm for all simulations. Aerosol diameter is set to 0.05, 0.5, and 5 μm for Aitken, accumulation, and coarse modes for corresponding simulations.



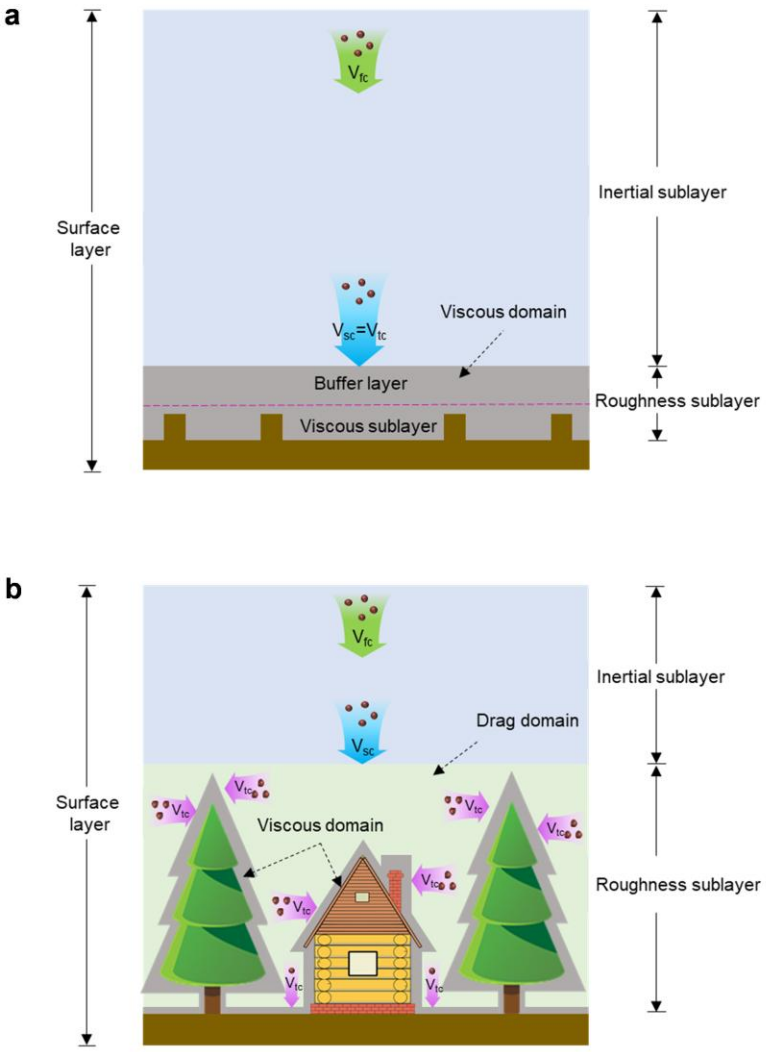

**Extended Data Fig. 5| The scale analysis of aerosol motion. a**, In viscous domain. **b**, In drag domain. **c**, In inertial sublayer. $\tau_{ae}$, $\tau_{te}$, $\tau_b$, $\tau_g$, and $\tau_{tur}$ are defined as the time required for the corresponding mechanisms (advection entrainment, turbulent entrainment, Brownian motion, gravitational settling and turbophoresis) to drive aerosols to move one meter. The larger the time scale, the less important the corresponding mechanism. Grey boxes show ignored mechanisms in reconstructing ADD physical framework.



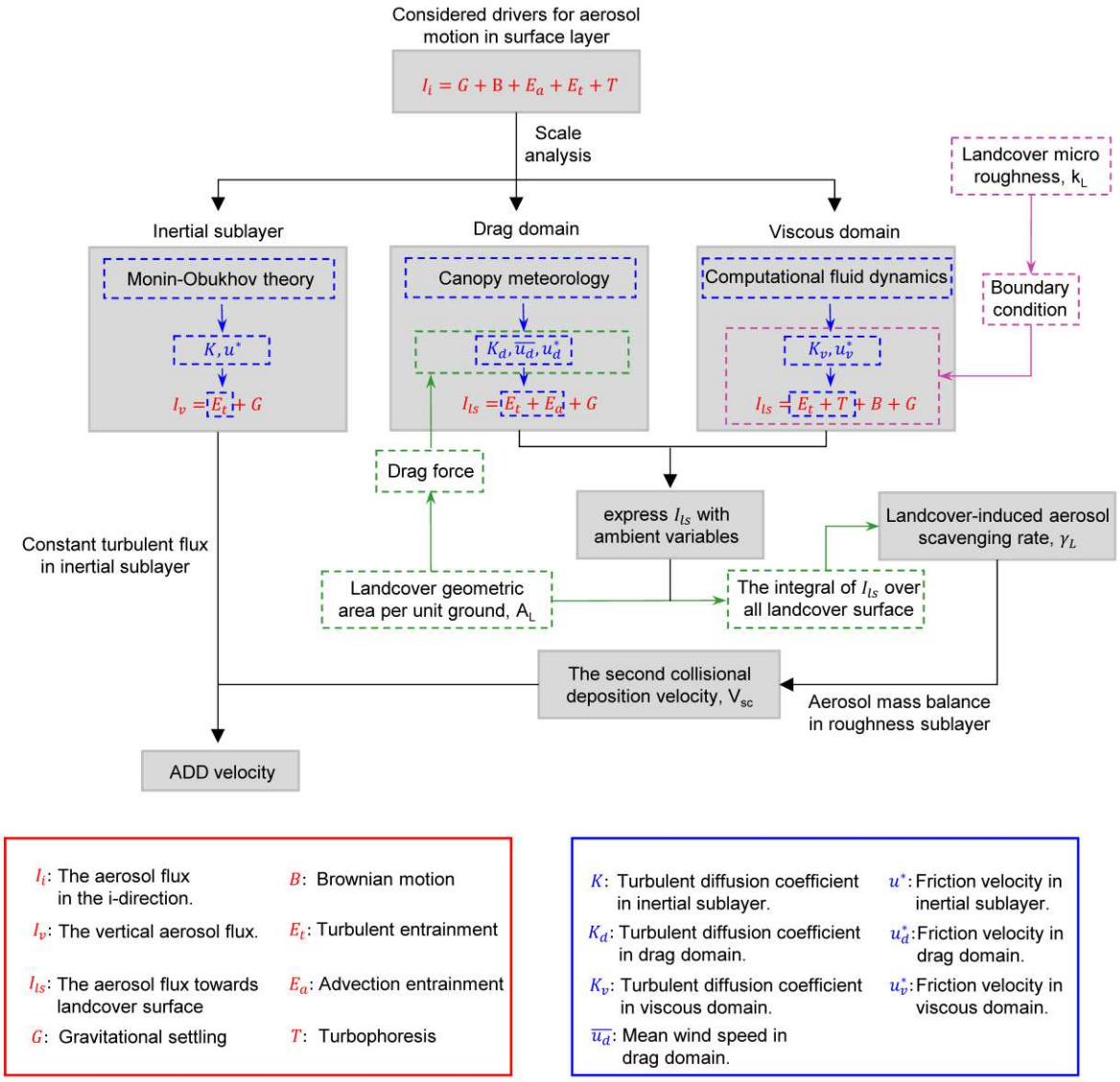

**Extended Data Fig. 6| The relationship between wind attenuation coefficient and landcover geometric area per unit ground. a**, For built-up land. **b**, For vegetated land. Observed wind attenuation coefficient β is calculated from measured wind profiles in wind tunnel experiments (**a**) and real forests (**b**). $\lambda_f$ refers to landcover front area per unit ground, which equals $2*A_V/\pi$ and $2*A_b/\pi$ for vegetated land and built-up land respectively (Supplementary, section 2).




**Extended Data Fig. 7| Multiple Influences of landcover geometry calculated based on the resistance model configured with refitted parameters. a**, Influence of landcover geometry on global ADD velocity. **b**, Relative changes of global column aerosol mass induced by landcover geometry (%). **c**, Absolute changes of global aerosol forcing induced by landcover geometry ($W/m^2$). **d**, Relative changes of global aerosol forcing induced by landcover geometry (%). These results are obtained by comparing the scenario considering landcover geometry predicted by PWM theory with the scenario ignoring landcover geometry predicted by the resistance model configured with refitted parameters. According to this calculation method, terrestrial aerosol cooling effect is reduced by 38%. Only the optimal estimation of multiple impacts of landcover geometry are presented here. The optimal estimation means input landcover geometry parameters meet: (1) values of $A_L$ are taken as averages of results calculated from different remote sensing data sets; (2) values of $k_L$ for ground, vegetations or buildings are taken as the optimal values that generate modeled ADD velocity agreeing best with observations within the measured $k_L$ range of corresponding materials.




**Extended Data Fig. 8| Illustration of $V_{fc}$, $V_{sc}$, and $V_{tc}$. a**, Situation for canopy-free landcover. Roughness sublayer in this case only includes viscous domain (grey area). **b**, Situation for canopy-containing landcover. Roughness sublayer in this case includes viscous domain (grey area) and drag domain (light green area).




**Extended Data Fig. 9| The outline of the derivation of ADD velocity.** Red symbols highlight the role of aerosol dynamics. Bule symbols and boxes highlight the role of multi-scale fluid dynamics. Green and pink boxes highlight the role of landcover geometry. See mathematic details in Supplementary.

## Supplementary Files

This is a list of supplementary files associated with this preprint. Click to download.

- Supplementary.docx